

Frontogenesis Elevates the Maximum Chlorophyll a Concentration at the Subsurface Near the Kuroshio During Well-Stratified Seasons

メタデータ	<p>言語: English</p> <p>出版者:</p> <p>公開日: 2024-02-14</p> <p>キーワード (Ja):</p> <p>キーワード (En): frontogenesis; subsurface chlorophyll maximum; in situ observation; satellite altimeter; the Kuroshio; mesoscale eddies</p> <p>作成者: 伊藤, 大樹, 児玉, 武稔, 清水, 勇吾, 瀬藤, 聡, 日高, 清隆, 安倍, 大介, 寒川, 清佳</p> <p>メールアドレス:</p> <p>所属: 水産研究・教育機構, 水産研究・教育機構 (退職), 現所属: 東京大学, 水産研究・教育機構, 水産研究・教育機構, 水産研究・教育機構, 水産研究・教育機構, 水産研究・教育機構</p>
URL	<p>https://fra.repo.nii.ac.jp/records/2000158</p>

Key Points:

- Frontogenesis supplies nutrients and increases subsurface chlorophyll *a* concentration
- Chlorophyll *a* concentration is positively correlated with the strength of fronts and frontogenesis
- Subsurface chlorophyll *a* concentration is estimated using satellite-derived geostrophic velocity

Correspondence to:

D. Ito,
ito_daiki41@fra.go.jp

Citation:

Ito, D., Kodama, T., Shimizu, Y., Setou, T., Hidaka, K., Ambe, D., & Sogawa, S. (2023). Frontogenesis elevates the maximum chlorophyll *a* concentration at the subsurface near the Kuroshio during well-stratified seasons. *Journal of Geophysical Research: Oceans*, 128, e2022JC018940. <https://doi.org/10.1029/2022JC018940>

Received 3 JUN 2022

Accepted 4 MAY 2023

Author Contributions:

Formal analysis: D. Ito, T. Kodama
Investigation: D. Ito, Y. Shimizu, T. Setou, K. Hidaka, D. Ambe, S. Sogawa
Methodology: D. Ito
Resources: Y. Shimizu, T. Setou
Validation: D. Ito
Writing – original draft: D. Ito
Writing – review & editing: T. Kodama, Y. Shimizu, T. Setou, K. Hidaka

Frontogenesis Elevates the Maximum Chlorophyll *a* Concentration at the Subsurface Near the Kuroshio During Well-Stratified Seasons

D. Ito¹ , T. Kodama^{1,2} , Y. Shimizu¹, T. Setou¹, K. Hidaka¹ , D. Ambe¹ , and S. Sogawa¹

¹Fisheries Resources Institute, Japan Fisheries Research and Education Agency, Yokohama, Japan, ²Now at Graduate School of Agricultural and Life Sciences, The University of Tokyo, Tokyo, Japan

Abstract The contribution that fronts and frontogenesis make to subsurface chlorophyll *a* (CHL) concentration was investigated near the Kuroshio using data from multiple surveys across the Kuroshio during summer and fall and satellite sea surface height (SSH) data alongside high-resolution reanalysis data set. An intensive survey was conducted during a period of frontogenesis as seen from the in-situ and satellite-derived velocity data as well as the analysis of the reanalysis data set. Physical and biological observation showed shoaling of the nitracline and a subsurface CHL maximum (SCM) near the evolving front. The CHL concentration at the SCM (CHL_{SCM}) was large near the front compared with the concentration in ambient water. Sections of 10 repeat seasonal surveys also captured the frontal structure, the shoaling of the nitracline, and the increase in CHL_{SCM} as well as their interrelationship. The CHL_{SCM} was large, and the depth of the SCM (Z_{SCM}) was shallow above a large horizontal density gradient (i.e., marked mesoscale frontal structure) in the ocean interior. In addition, we demonstrate that the lateral strain rate, which is a measure of frontogenesis obtained from the SSH, can be used to estimate Z_{SCM} and CHL_{SCM}. Frontogenesis, secondary circulation, symmetric instability, and vertical diffusion were considered to cause the nutrient supply to the subsurface layer. The surveys and analysis indicate that fronts and frontogenesis increase CHL_{SCM}, and the physical data obtained from both in-situ and satellite observations can be used to estimate CHL distribution in the ocean interior.

Plain Language Summary The contribution that oceanic front and its strengthening make to subsurface chlorophyll *a* (CHL) concentration was investigated near the Kuroshio south of Japan using data from multiple surveys and satellite altimetry alongside high-resolution reanalysis data set. The Kuroshio front strengthened during an intensive survey across the Kuroshio as seen from in-situ, satellite-derived and reanalysis velocity data. Physical and biological observations showed nutrient upwelling and increase in subsurface chlorophyll *a* concentration near the strengthening front. Sections of 10 repeat surveys during summer and fall showed that the depth where the chlorophyll *a* concentration increased was shallow and the chlorophyll *a* concentration was large when the front was strong. In addition, we demonstrate that a measure of strengthening of fronts obtained from the satellite-derived data is valid to estimate the distribution of subsurface chlorophyll *a* concentration.

1. Introduction

Satellite images of the sea surface show that oceanic fronts, where water masses with different physical and biogeochemical properties meet, are always associated with gyres and mesoscale eddies (e.g., Munk et al., 2000). The heterogeneous environments that are produced by fronts are important for marine life and fisheries (Claustre et al., 1994; Mahadevan, 2016; Saitoh et al., 1986; Sugimoto & Tameishi, 1992; Videau, 1987). Fronts can be identified as a surface band on the water, made visible because of the higher concentrations of suspended solids (Munk et al., 2000; Uda, 1938; Yanagi, 1987). The experimental and theoretical study of frontogenesis, the generation and evolution of fronts, is well established (Hoskins, 1982; Miller, 1948). Following progress in modeling and monitoring techniques in recent decades, the effect of frontogenesis on biogeochemistry has been studied as part of research into submesoscale ($O(1-10$ km)) phenomena (McWilliams, 2016; Tandon & Nagai, 2019; Thomas et al., 2008).

Frontogenesis is often associated with mesoscale ($O(100$ km)) eddies and fronts. Recent numerical models have revealed the importance of frontogenesis in both dynamical processes (Capet et al., 2008a, 2008b, 2008c; Gula et al., 2014; Lapeyre & Klein, 2006; McWilliams et al., 2009; Mensa et al., 2013; Sasaki et al., 2014)

and rapid primary productivity (Klein & Lapeyre, 2009; Lévy et al., 2012, 2018; Mahadevan, 2016; Perruche et al., 2011; Smith et al., 2016). For example, the vertical transport of nutrients via frontogenesis-enhanced upwelling can increase chlorophyll *a* (CHL) concentrations near fronts (Klein & Lapeyre, 2009; Lévy et al., 2012; Mahadevan, 2016; Perruche et al., 2011). Direct microstructure measurements have also shown that active turbulent mixing near frontal structures increases the vertical transport of nutrients (Hales et al., 2009; Kaneko et al., 2013). At the same time, CHL concentrations increase due to passive process (e.g., mesoscale stirring) that existing biological features are accumulated by submesoscale currents (Lévy et al., 2018).

The Kuroshio is one of the main oceanic fronts and a western boundary current of the North Pacific subtropical gyre, which is bordered by a shallow pycnocline inshore, between the Kuroshio and the south coast of Japan. Despite being subtropical, the inshore region is characterized by relatively nutrient-rich water in the surface layer (Komatsu & Hiroe, 2019). In addition, the evolution of the Kuroshio front induces local nutrient upwelling (Kaneko et al., 2013; Kimura et al., 1997; Kimura et al., 2000) in common with other frontal regions, such as the Gulf Stream (Hales et al., 2009; Yoder et al., 1981) and at the periphery of mesoscale eddies (Lévy et al., 2001; Mahadevan et al., 2008). Several in-situ observations near the Kuroshio have shown that turbulent mixing is caused by submesoscale phenomena such as frontogenesis, resulting in a secondary circulation (Nagai et al., 2009), and symmetric instability (SI) (D'Asaro et al., 2011). The secondary circulation is a closed circulation with upwelling (downwelling) on the less (more) dense side of evolving fronts. Moreover, internal waves likely trapped in the Kuroshio front also enhance turbulent mixing near the jet (Kaneko et al., 2012; Nagai et al., 2012). These processes on scales smaller than mesoscale supply nutrients to the euphotic layer (Kaneko et al., 2013; Nagai & Clayton, 2017; Nagai et al., 2017; Nagai et al., 2019).

The nutrients supplied by these processes should support primary production and subsequent biological and fishery production near the Kuroshio, which is the main spawning and nursery ground for commercial pelagic fish (Sugisaki et al., 2010; Takasuka et al., 2008, 2014; Okazaki et al., 2019). In fact, a subsurface CHL maximum (SCM) usually appears in well-stratified seasons (i.e., summer and fall) near the Kuroshio (e.g., Takahashi et al., 1985). The SCM is common in the subtropics (Saijo et al., 1969) due to depletion of surface nutrients, and is typically observed near the base of the euphotic zone, which often coincides with the nitracline (Cullen & Eppley, 1981) because of the upward flux of nutrients (Cullen, 2015). Variations in the distribution of the nutrient supply will affect the degree to which the SCM develops. The importance of the SCM in biological production varies seasonally; the SCM has a particularly large impact on primary production during summer and fall (Goericke & Welschmeyer, 1998; Masuda et al., 2010; Richardson et al., 2000; Sharples et al., 2001; Weston et al., 2005).

The CHL concentration of SCM (CHL_{SCM}) is likely to be heterogeneous and elevated episodically near the front, because the nutrient supplies determine both the CHL_{SCM} and its depth (Z_{SCM}). However, there are few in-situ observations of the SCM's distribution in relation to fronts. In addition, although the CHL_{SCM} has been predicted using an optical model (Morel, 1988), few studies have estimated CHL_{SCM} using physical observations, such as hydrographic sections and satellite sea surface height (SSH) maps despite the importance of the SCM in primary production. In this study, an intensive summer survey was conducted near the Kuroshio to examine the conditions under which CHL_{SCM} increased due to the mesoscale front and frontogenesis. The process of submesoscale phenomena was diagnosed using a high-resolution ocean reanalysis data set. In addition, repeat seasonal surveys across the Kuroshio and SSH data were analyzed to evaluate increases in CHL_{SCM} associated with the mesoscale variation of the front both at the surface and in the interior. Our data clarify the role that fronts and frontogenesis play in SCM distribution.

2. Materials and Methods

In this study, several different materials and methods were used for meso-to submesoscale phenomena. The intensive survey data resolved mesoscale, and contained traces of smaller-scale phenomena. The seasonal repeat surveys had similar features although their horizontal resolution was lower than that of the intensive survey. The SSH data set also showed the mesoscale distribution patterns of water mass. These data were used for a linear model analysis to examine the contribution of dynamical processes to the CHL distribution. In addition, the output of a numerical experiment driven by the horizontal velocities calculated from SSH well described submesoscale feature. The high-resolution ocean reanalysis data set was partially submesoscale-resolving, and was used to examine the temporal evolution of the front.

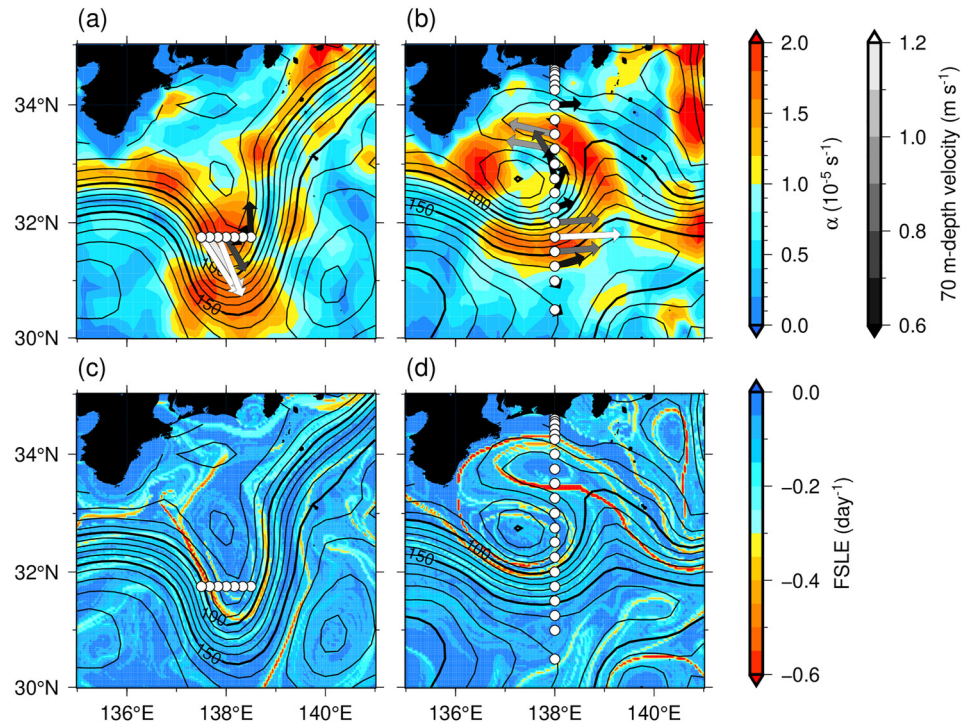


Figure 1. Locations of CTD stations (open circles) for (a, c) the intensive survey and (b, d) the observation along 138°E in August–September 2017 as an example of the repeat survey. Colors denote (a, b) α (10^{-5} s^{-1}) and (c, d) Finite-size Lyapunov exponent (day^{-1}) on 26 August 2019 and 24 August 2017, respectively. Thin and thick black lines denote satellite sea surface height with a contour interval of 10 and 50 cm, respectively. Colored arrows in (a) and (b) denote the horizontal velocity (m s^{-1}) at 70-m depth observed ADCP.

2.1. Intensive Survey

The intensive survey was conducted on 26 August 2019 (Ito et al., 2023a, 2023b), using the R/V *Soyo-maru* along 31°50'N across the Kuroshio (Figure 1a). The Kuroshio had a large meander (Kawabe, 1985, 1995) in the summer of 2017, and the western side of the meander crest was observed. Stations were set every 10 min in longitude. At each station, temperature (T), salinity (S), dissolved oxygen (DO), and fluorescence were measured by a conductivity–temperature–depth (CTD) profiler (Sea-Bird Scientific SBE 9plus) with a DO profiler (SBE43) and a fluorometer (Seapoint Sensors Inc.) from the surface to 200-m depth. In addition, T and S in the lower layer were obtained by an expendable CTD (XCTD; Tsurumi Seiki Co. Ltd., type 4) to a depth of 1,850 m, taken at the same location as the CTD. All casts were completed in 12 hr. Potential temperature (θ), potential density (σ_θ), and buoyancy were calculated from T and S obtained by the CTD/XCTD. Buoyancy was derived as:

$$b = -g\rho/\rho_0, \quad (1)$$

where g is the gravitational acceleration and ρ is the density anomaly from the mean density ρ_0 . Northward and eastward current velocities (u and v , respectively) were measured continuously with a shipboard RDI 75-kHz acoustic Doppler current profiler (ADCP) at depth intervals of 16 m. The data were calibrated for angle misalignment using bottom tracking data (Joyce, 1989). The ship velocities were measured using the Global Positioning System. Current velocity profiles were estimated at intervals of 5 min and an average for each CTD station was taken from the seven profiles.

Discrete water samples were collected vertically using Niskin bottles mounted on the CTD with a carousel multiple sampling system. Nutrient concentrations, nitrate plus nitrite, nitrite, phosphate, and silicate concentrations were measured on shore in a laboratory by colorimetric method using an autoanalyzer (QuAAtro39; BL TEC) (Kodama et al., 2014). Hereafter, only nitrate concentrations are shown because nitrogen is the potential limiting nutrient for primary production in the Kuroshio and nitrate is the dominant nitrogenous species (Kodama et al., 2014, 2015). We defined the 1- μM -nitrate isoconcentration as the nitracline and made this a

Table 1
List of the Repeat Observation Cruise Dates in Summer and Fall

Year	Summer	Fall
2014	August 22nd–September 3rd	October 23rd–November 4th
2015	August 21st–September 2nd	October 23rd–November 4th
2016	August 24th–September 5th	October 26th–November 6th
2017	August 22nd–September 1st	November 7th–17th
2018	August 23rd–September 2nd	November 8th–18th

focus of the study (e.g., Cullen & Eppley, 1981). The CHL concentration was measured by analyzing 250 mL of seawater on shore fluorometrically (Welschmeyer, 1994) using a fluorometer (10AU Field and Laboratory Fluorometer; Turner Design) after extraction in N, N-dimethylformamide (Suzuki & Ishimaru, 1990). Here, we show the analyzed CHL concentration, rather than the concentrations obtained from the mounted fluorometer.

The NO value was calculated from DO and nitrate data based on Broecker (1974):

$$\text{NO} = 9 \times [\text{Nitrate}] + [\text{DO}]. \quad (2)$$

The NO value is nearly conservative at subsurface layers without air-sea oxygen exchange because the variation of nitrate during respiration and photosynthesis is compensated by that of DO. We also estimated diffusive upward nitrate flux (F) as:

$$F = \frac{\Gamma \varepsilon}{b_z} N_z, \quad (3)$$

where Γ , ε , b_z , and N_z are the mixing ratio, turbulent energy dissipation rate, and the vertical gradient of b and nitrate, respectively; $\Gamma \varepsilon / b_z$ is the vertical diffusivity according to Osborn (1980). We assumed that Γ and ε was 0.2 (Osborn, 1980) and $10^{-8} \text{ m}^2 \text{ s}^{-3}$ (Kaneko et al., 2012; Kodama et al., 2014), respectively, although ε has considerable spatiotemporal variation.

2.2. Seasonal Repeat Surveys

The repeat seasonal surveys were carried out between 34°45'N and 28°N along 138°E (called the O-line) aboard the R/V *Soyo-maru* (Figure 1b). The surveys were conducted five times a year from 2014 to 2018. We analyzed the summer and fall cruise data (Table 1) because strong stratification and associated SCM only develops in these seasons. The CTD stations and water sampling points were typically set at every 15–30 miles (Figure 1b). Horizontal velocities were measured continuously using the ADCP. The data and water samples were processed using the same methods as in the intensive survey data. In addition, a horizontal gradient of b along the meridional observation line (b_y) was calculated to identify the fronts. To estimate location and strength of the front, the maximum value of absolute b_y in a profile ($b_{y \text{ max}}$) was determined as the largest maximum value of absolute b_y from three profiles: the profile itself and the two neighboring profiles. This was done to consider the horizontal extent of the fronts and the dynamical processes associated with the fronts. The values of $b_{y \text{ max}}$ were calculated at offshore stations where bathymetry was $\geq 1,000 \text{ m}$ to eliminate the influence of coastal water on the density gradient.

2.3. Satellite Observation

We used the absolute SSH data set produced and distributed by the Copernicus Marine and Environment Monitoring Service (<https://marine.copernicus.eu/>) provided on a $1/4^\circ \times 1/4^\circ$ grid to detect the location of fronts, and evolving fronts in particular. The lateral strain rate (α) was used as a measure of the deformation of fronts including frontogenesis. The rate is derived as:

$$\alpha = [(U_x - V_y)^2 + (V_x + U_y)^2]^{1/2}, \quad (4)$$

where U and V are zonal and meridional velocities deduced from SSH as $U = -(g/f_0)h_y$ and $V = (g/f_0)h_x$, h and f_0 are SSH and the Coriolis parameter, respectively, x and y are zonal and meridional coordinates (positive eastward and northward), and subscripts denote derivatives. The value of α calculated from SSH was large near the Kuroshio and eddies and was estimated to be $1.6 \times 10^{-5} \text{ s}^{-1}$ in the observed area (Figures 1a and 1b). The value of α in the observed area was consistent with the value reported for frontogenesis driven by mesoscale confluence in numerical models (Thompson, 2000) and observations (Rudnick, 1996; Nagai et al., 2009); that is, the SSH field suggested the evolution of the fronts in the observed area.

Finite-size Lyapunov exponent (FSLE) was used to identify regions where the surface stretching driven by altimetry-detected mesoscale structure was strong. FSLE is a Lagrangian feature and the separation of a pair of initially close particles forced by the satellite-observed flow field (d'Ovidio et al., 2004). The magnitude of

the separation is defined as the largest eigenvalue (λ) of FSLE, $\lambda(d_0, d_f) = \tau^{-1} \log(d_f/d_0)$, where d_0 and d_f is the initial and final separation distance, respectively, and τ the first time when the separation distance reached d_f . We used the $1/25^\circ \times 1/25^\circ$ grid delayed-time FSLE value-added product provided by AVISO (<https://www.aviso.altimetry.fr/es/data/products/value-added-products/fsle-finite-size-lyapunov-exponents.html>). FSLE is calculated backward in time (i.e., λ has negative values) using $d_0 = 0.02^\circ$ (approximately 2 km) and $d_f = 0.6^\circ$ (approximately 66 km). Large negative values of λ indicate regions of strong stretching. The relation between FSLE and submesoscale fronts has been demonstrated in previous studies (e.g., Siegelman et al., 2020).

We used a data set of the Kuroshio axis provided by the Japan Coast Guard (<https://www1.kaiho.mlit.go.jp>) to estimate the positions of the CTD stations relative to the Kuroshio since the inshore region of the Kuroshio is characterized by relatively nutrient-rich water in the surface layer (Komatsu & Hiroe, 2019). The Kuroshio axis is determined by synthetic analyses of satellite data alongside in-situ observations. The distance in degrees from the Kuroshio axis at 138°E (D_K) was calculated for each CTD station. Positive and negative values of D_K denote the distance to the south and north, respectively.

2.4. Empirical Model Analyses

An empirical model (generalized linear model; hereafter GLM) analysis was performed to verify the significant contribution of the temporal change in the fronts (α) to the CHL distribution. We set Z_{SCM} as the objective variable, and the following variables as the explanatory variables (Equation 5). D_K is the distance from the Kuroshio axis. The Kuroshio axis is one of the boundaries of the ocean conditions including the depth of SCM (Kodama et al., 2014). The values of $b_{y_{\text{max}}}$ was an indicator of the location and strength of the front from in-situ observations. The values of α examined temporal change in the fronts including frontogenesis obtained from satellite altimeter. The SSH was an index of the mesoscale structure. The error distribution of Z_{SCM} is assumed as the Gamma distribution, and the straight-linear-link function was used in the GLM. The full model is as follows:

$$Z_{\text{SCM}} = \text{glm}(\text{SSH} + b_{y_{\text{max}}} + \alpha + D_K + \beta), \quad (5)$$

where β is the intercept. The variance inflation factor of the explanatory was smaller than 3.4, and the explanatory variables were selected by Akaike information criterion (AIC). The fitting of the model were evaluated with deviance explained (DE; $100 \times (1 - \text{residual deviance}/\text{null deviance})$). The explained proportion of the remained parameters after AIC selection was evaluated with the difference of DE from the least-AIC model and those in which the target explanatory variable was removed (ΔDE).

The other GLM which used the depth of the nitracline (Z_{N_1}) instead of SSH was performed to verify the significant contribution of (α) in the relationship between Z_{SCM} and Z_{N_1} . The relationship between Z_{SCM} and Z_{N_1} was expected to correlate strongly. However, when the other parameters' contribution was significant, nitrate supply from the lower layer would be strong. The full model is as follows:

$$Z_{\text{SCM}} = \text{glm}(Z_{\text{N}_1} + b_{y_{\text{max}}} + \alpha + D_K + \beta). \quad (6)$$

The other manners were same as those of Equation 5.

2.5. Reanalysis Data Set

We used the MOVE/MRI. COM-JPN data set for the period of the intensive survey (26 August 2019) derived from the Japanese Coastal Ocean Monitoring and Forecasting System (Hirose et al., 2019, 2020) developed by the Meteorological Research Institute (MRI). The surface boundary conditions were given by the 3-hourly JRA55-do data set (Tsujino et al., 2018). The output used in this study has a resolution of $1/33^\circ$ zonally and $1/50^\circ$ meridionally (about 2 km). Details of the assimilative simulation were described by Hirose et al. (2019).

The surface lateral strain rate was calculated using Equation 4 from SSH in the reanalysis data set. The geostrophic velocities were derived by subtracting the SSH at approximately 15 km intervals. In addition, the lateral strain rate in the ocean interior was calculated by replacing U and V in Equation 4 with the data set of u and v . To examine

the evolution of the horizontal velocity field and frontogenesis, we calculated the time evolution of the horizontal buoyancy gradient as follows (Hoskins, 1982):

$$\frac{D}{Dt} \nabla b = \begin{bmatrix} -u_x b_x - v_x b_y \\ -u_y b_x - v_y b_y \end{bmatrix} \equiv \begin{bmatrix} Q_1 \\ Q_2 \end{bmatrix} = \mathbf{Q}, \quad (7)$$

where b is considered to be forced by a horizontal two-dimensional, nondivergent flow. The components of \mathbf{Q} -vector Q_1 and Q_2 contribute to the temporal evolution of the frontal structure in the zonal and the meridional direction, respectively. The frontal tendency was evaluated by the change of the amplitude of the buoyancy gradient (T_F) defined in Hoskins (1982) as:

$$T_F = \frac{1}{2} \frac{D}{Dt} \|\nabla_h b\|^2. \quad (8)$$

The positive and negative values of T_F indicate the evolution and decay (frontolysis) of the fronts, respectively. The condition for SI is diagnosed by values of Ertel's potential vorticity ($PV < 0$) (Hoskins, 1974; Thomas et al., 2013, 2016). We calculated a modified form of the parameter that evaluates the condition for SI given in Itoh et al. (2022) as follows:

$$q^{-1} = \left(1 + \frac{v_x - u_y}{f} \right)^{-1} \text{Ri}^{-1}, \quad (9)$$

where $\text{Ri} = b_z / (u_z^2 + v_z^2)$ is the Richardson number. The condition for SI ($PV < 0$) corresponds to $q^{-1} > 1$.

3. Results

3.1. Intensive Survey

Warm ($\theta > 18^\circ\text{C}$) and saline ($S > 34.8$) subtropical water was observed at depths of 100–250 m (23.0 – $25.2\sigma_\theta$) in the western half of the section (Figures 2a and 2b). On the eastern side, warm water in the 23.0 – $25.2\sigma_\theta$ layer was thin and fresh compared with that in the west, and the surface water was fresher ($S < 34$). These adjacent water masses form a clear front extending from 50 to 600 m, as seen from density gradients in the western half of the section (Figures 2a and 2b). At the front, a strong southeastward flow ($>1.3 \text{ m s}^{-1}$) was observed near the surface to the west of $137^\circ40'\text{E}$ (Figures 2c and 2d). This southeastward jet and the northwestward flow east of $138^\circ20'\text{E}$ form a cyclonic feature corresponding to the crest of a large meander in the Kuroshio. The southeastward jet at a depth of 70 m was zonally confluent around $137^\circ50'\text{E}$ (arrows in Figure 1a), which supports the interpretation that the front was in the process of frontogenesis.

The nitrate was depleted above the nitracline defined as the $1\text{-}\mu\text{M}$ -nitrate isoconcentration regardless of the distance from the Kuroshio front (Figure 2e). The nitracline was approximately consistent with the maxima of N_z especially east of the front (Figures 2e and 2f). In the west of the front, the values of N_z were not large with the horizontal slope of the nitracline. The distribution of nitrate follows the potential density distribution in the east of the front (Figures 2e and 2f); the nitracline was along the $24.8\sigma_\theta$ isopycnal (around a depth of 100 m). The apparent oxygen utilization (AOU) was low above the nitracline at 40–80 m (Figures 2e–2g), and the CHL concentration was large below the low-AOU water following the nitracline (Figures 2e–2h), suggesting the increase of DO through photosynthesis. In contrast, in the frontal region around $137^\circ50'\text{E}$, nitrate isolines were convex upward across isopycnals with a horizontal scale of $<30 \text{ km}$ (Figures 2e and 2f). The AOU was high ($\sim 70 \mu\text{mol L}^{-1}$) in this water (Figure 2g) probably because of the upwelling from greater depths. A particularly high CHL_{SCM} ($\sim 0.5 \mu\text{g L}^{-1}$) was observed immediately above the convex nitracline at depths of 40–70 m (Figure 2h). The high CHL_{SCM} was located in the large- α area (Figure 1a) and near but not just below the large-FSLE (Figure 1c). The nitrate and CHL distribution indicate the shoaling of the nitracline and an increase in CHL_{SCM} near the Kuroshio front ($<138^\circ\text{E}$).

The nitracline east of 138°E was clearly distinguishable following a potential density of $24.8\sigma_\theta$, above which nitrate was depleted (Figure 3a). This low-nitrate water was a correspondingly low AOU (Figure 3b). The NO value (Figure 3c) in this region was high ($>200 \mu\text{mol L}^{-1}$) due to the low AOU (i.e., high DO concentrations). In contrast, immediately west of 138°E , NO values of $200 \mu\text{mol L}^{-1}$ were found in the $24.0\sigma_\theta$ layer corresponding to the high-nitrate and low-AOU water, which had a convex upward shape, and in the deeper layer outside the front (Figures 3a–3c). The high CHL_{SCM} followed the nitrate shape (Figure 3d). To the west of 138°E , the high NO

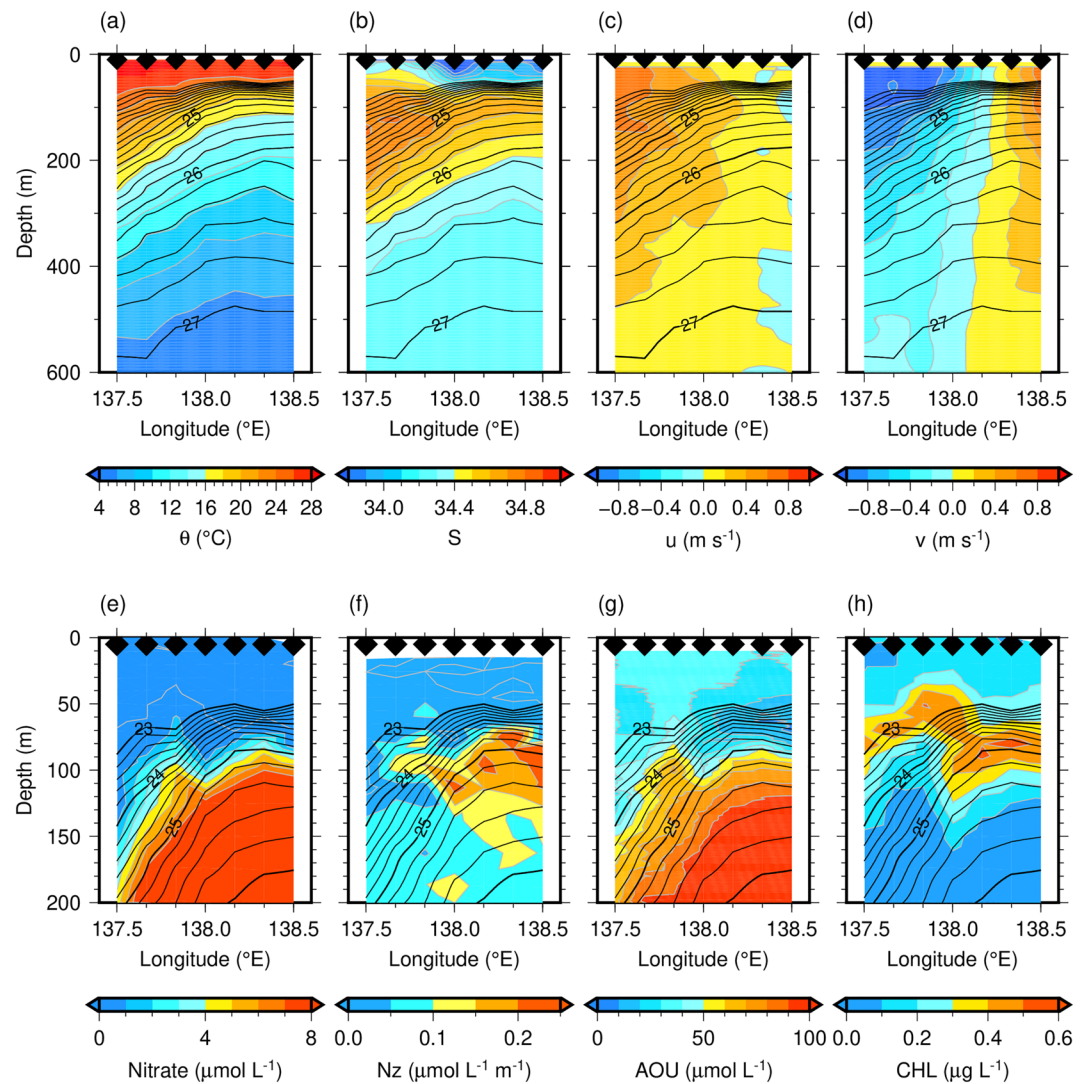


Figure 2. Sections of (a) θ (°C), (b) S , (c) u (m s⁻¹), (d) v (m s⁻¹), (e) nitrate ($\mu\text{mol L}^{-1}$), (f) N_z ($\mu\text{mol L}^{-1} \text{m}^{-1}$), (g) AOU ($\mu\text{mol L}^{-1}$), and (h) CHL ($\mu\text{g L}^{-1}$) along 31°50'N on 26 August 2019. Black diamonds at the top of the panel indicate the locations of CTD stations. Black lines denote σ_θ with a contour interval of 0.2 kg m⁻³ from 23 to 27 kg m⁻³.

value was caused by high nitrate rather than low AOU (Figures 3a–3c). Considering that NO values are conserved without air–sea oxygen exchange, high-NO water must be supplied from greater depths to the shallower layer near the front.

The diapycnal supply of high-NO water suggested strong turbulent vertical mixing and resulting nitrate flux. We calculated F for the convex upward nitracline (137°50'E at a depth of 90 m) using Equation 3. The estimated value was $1.1 \times 10^{-6} \text{ mmol N m}^{-2} \text{ s}^{-1}$, which is of an order of magnitude larger than that calculated at the same depth outside the Kuroshio front and of the same order at the nitracline east of 138°E, where N_z was large due to the mesoscale cyclonic feature. The large nitrate flux near the front was suggested although the turbulence intensity has a large spatiotemporal variation.

3.2. Reanalysis Data Set

The reanalysis data set showed water mass and velocity distribution consistent with the intensive observations. A map of surface α had a higher resolution than that obtained by satellite altimeter, but a similar distribution relative to the Kuroshio front (Figures 1a and 4a). West of 138°E, satellite-based (Figure 1a), reanalysis surface (Figure 4a)

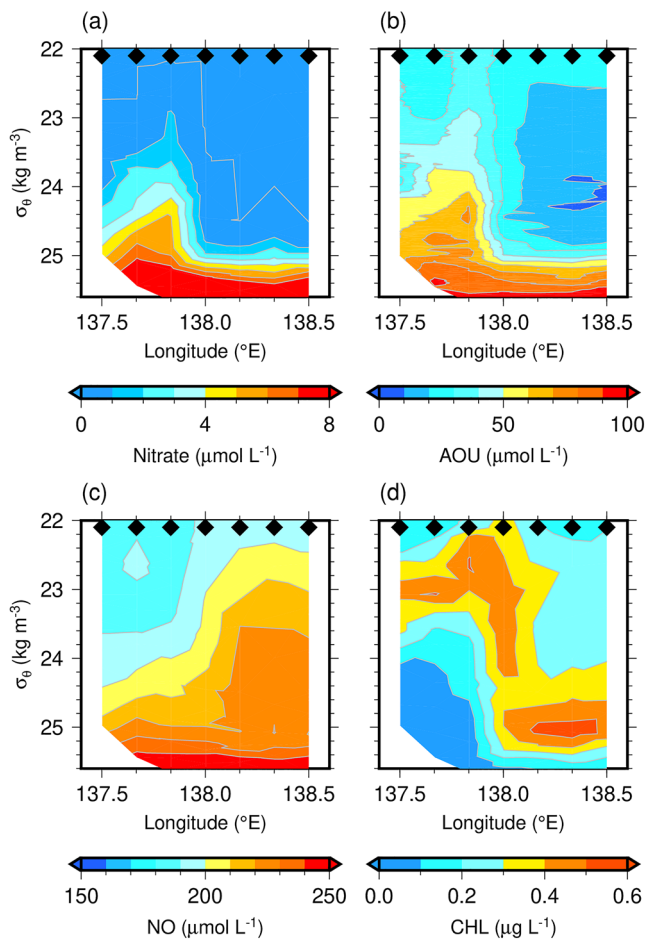


Figure 3. Distributions of (a) nitrate ($\mu\text{mol L}^{-1}$), (b) AOU ($\mu\text{mol L}^{-1}$), (c) NO ($\mu\text{mol L}^{-1}$), and (d) CHL ($\mu\text{g L}^{-1}$) along 31°50'N. Black diamonds at the top of the panel indicate the locations of CTD stations.

and 100-m depth (Figure 4c) α showed large values inside the Kuroshio front (approximately along 110–120 and 40 cm contours, respectively). East of 139°E, these were large along the inside (110–120 and 40 cm) and outside (140–150 cm and 90–100 cm) of the Kuroshio front. In the bended region between 138 and 139°E, these values were large over a wide area from the inside to the outside the Kuroshio front. These similarity suggest the validity of the identification of the interior strain field using SSH. The temperature distribution at a depth of 100 m clearly showed the contrast between the Kuroshio and the inshore region (Figure 4b). The Kuroshio front, which consisted of warm and saline subtropical water and cold and fresh inshore water and generated a strong southeastward flow, was also consistent with that found in the intensive survey (Figures 2a–2d and Figures 5a–5d).

Since the Kuroshio front was roughly along meridians, there was a strong negative b_x and relatively weak negative b_y in the observed area (Figures 4d, 4e, and 5e, 5f). Focusing on the evolution of the zonal gradient, b_x increases due to the convergent flow in the cross-front direction ($u_x < 0$) and the tilting of b_y by the shear flow (v_x), as seen from Q_1 in Equation 7. The values of u_x and v_x were negative and positive in the observed frontal area, respectively (Figures 4f, 4g, and 5g, 5h); that is, they acted to increase and decrease the negative b_x because the stretching ($-u_x b_x$; $u_x < 0, b_x < 0$) and tilting term ($-v_x b_y$; $v_x > 0, b_y < 0$) was negative and positive, respectively. The net forcing, Q_1 , contributed to the increase of negative zonal buoyancy gradient ($Q_1 < 0$; Figures 4h and 5i). The region where the negative b_x grew due to the deformation flow (Figures 4h and 5i) largely detected by α (Figures 4c and 5j).

While the negative b_y slightly decreased ($Q_2 > 0$; Figure 4i), the frontal tendency (T_F) was positive in the observed frontal area (Figures 4j and 5k) because of the large increase of negative b_x ($Q_1 < 0$; Figure 4h). The positive T_F supports the interpretation that the Kuroshio front was in the process of frontogenesis during the intensive survey. In contrast, negative values of T_F were found in downstream of the observed area, indicating a weakening of the front. The distribution of these large negative and positive T_F values was similar to that of large α values (Figures 1a, 4c, and 4j), and were located along the large FSLE values near the Kuroshio front with horizontal extent (Figure 1c).

The parameter q^{-1} indicated a modest contribution of SI. In the frontal region, specifically in the vicinity of 137°50'E at a depth of 100, an enhancement of $q^{-1} > 0.1$ was found. This location corresponded to the area where values of N_z (Figure 2f) and NO (Figure 3c) were locally increased. Additionally, the core of large q^{-1} was west of observed area in the lower layer centered at 137°20'E at a depth of 300 m (Figure 5l). The values of q^{-1} were about 0.3 at most and did not reach 1 in the core.

3.3. Repeat Surveys

The intensive survey around the Kuroshio showed shoaling of the nitracline accompanying an increase in the CHL_{SCM} . Similar structures are likely to be identified in repeat hydrographic surveys because the surveys have repeatedly traversed the front. We inspected sections of all 10 repeat surveys to confirm whether the large CHL_{SCM} and shallow Z_{SCM} near the front was captured. Here, we show the sections from August 2017 as a characteristic example of the distribution of physical and biological data from the surveys (Figure 6). In this period, the Kuroshio flowed around 31°45'N at the 138°E associated with the large meander (Figure 1b), and an anticyclonic eddy pinched off from the Kuroshio in the inshore region, with its center at 33°45'N, 137°30'E. The eddy appears as zonally elongated SSH contours from the northward flow at the eastern side of the large meander around 139°E (Figure 1b). The values of α along 138°E were large ($> 1.6 \times 10^{-5} \text{ s}^{-1}$) around 32° and 33°N along 138°E corresponding to the Kuroshio and the southern periphery of the anticyclonic mesoscale eddy, respectively

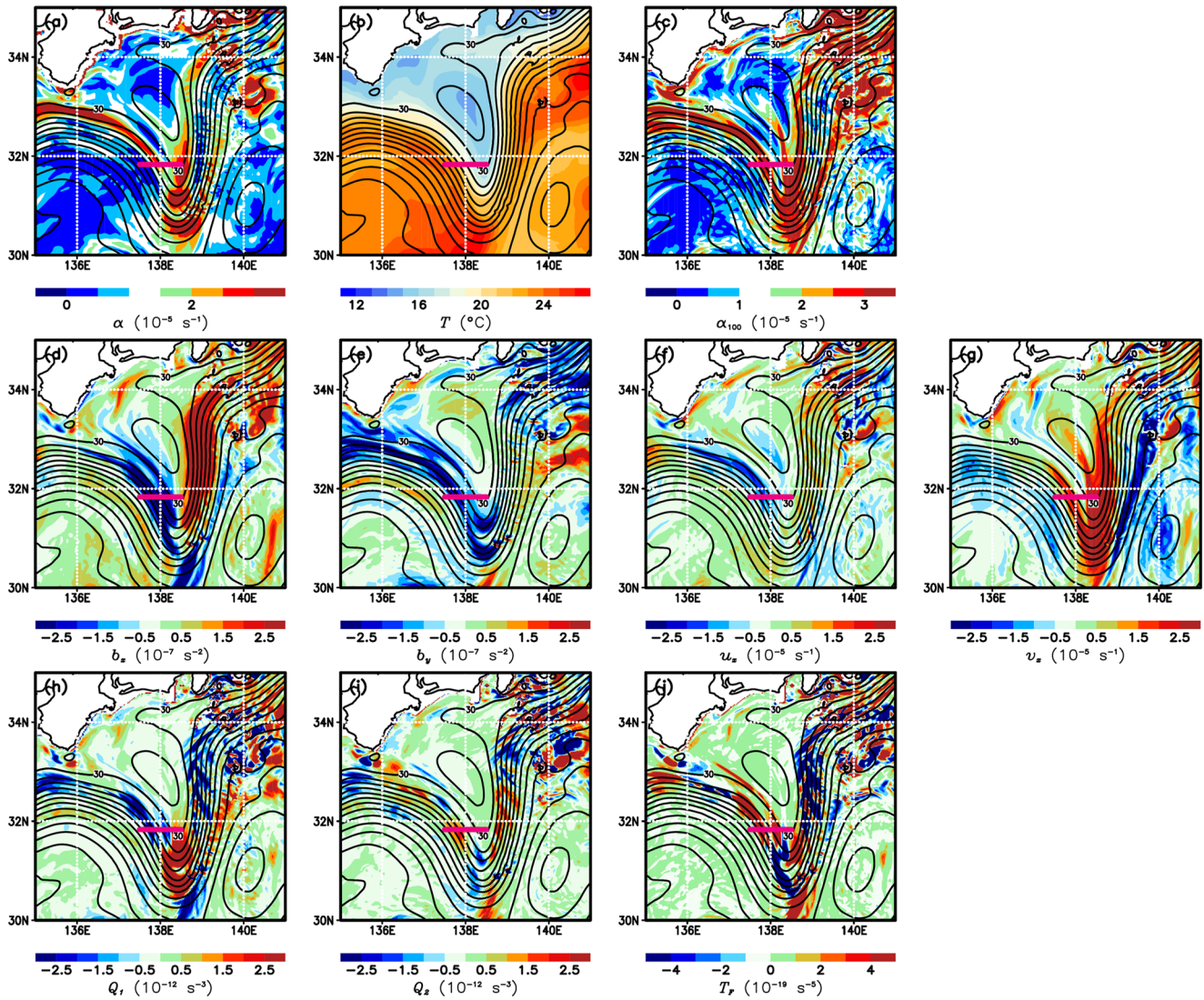


Figure 4. Distribution of (a) surface α (10^{-5} s^{-1}), (b) T ($^{\circ}\text{C}$), (c) α (10^{-5} s^{-1}), (d) b_x (10^{-7} s^{-2}), (e) b_y (10^{-7} s^{-2}), (f) u_x (10^{-5} s^{-1}), (g) v_x (10^{-5} s^{-1}), (h) Q_1 (10^{-12} s^{-3}), (i) Q_2 (10^{-12} s^{-3}), and (j) T_F (10^{-19} s^{-5}) at a depth of 100 m in the reanalysis data set. Black lines denote satellite sea surface height with a contour interval of 10 cm. Magenta line denotes the observed area in the intensive survey.

(Figure 1b). In addition, submesoscale structures were identified as large FSLE values along the Kuroshio front and the periphery of the anticyclonic mesoscale eddy (Figure 1d).

The 138°E section crossed the Kuroshio front around $31^{\circ}45'\text{N}$, where isopycnal slopes were steep, and the anticyclonic mesoscale eddy between $33^{\circ}15'$ and $34^{\circ}15'\text{N}$, which showed a typical bowl-shaped structure. Saline ($S > 34.8$) subtropical water was found in the $23.0\text{--}25.2\sigma_{\theta}$ layer south of the Kuroshio front and in the interior of the eddy inshore (Figure 6a). Between the Kuroshio and the southern periphery of the anticyclonic mesoscale eddy (between $31^{\circ}45'$ and $33^{\circ}15'\text{N}$), isopycnals were convex upward, and the water mass in the $23.0\text{--}25.2\sigma_{\theta}$ layer was fresh and thin, corresponding to typical inshore water (Kodama et al., 2014; Komatsu & Hiroe, 2019). In addition, especially fresh ($S < 34$) surface water typical of inshore water during summer was identified. The southern and northern fronts at the periphery of the eddy (around $33^{\circ}15'$ and $34^{\circ}15'\text{N}$, respectively) and the Kuroshio front (around $31^{\circ}45'\text{N}$) were identified as large positive and negative b_y values at depths of 100–500 m, with a maximum near 300 m (Figure 6b). In contrast, the surface layer (above a depth of 100 m) had large b_y values with the opposite sign to that of the lower layer due to fresh surface water from inshore.

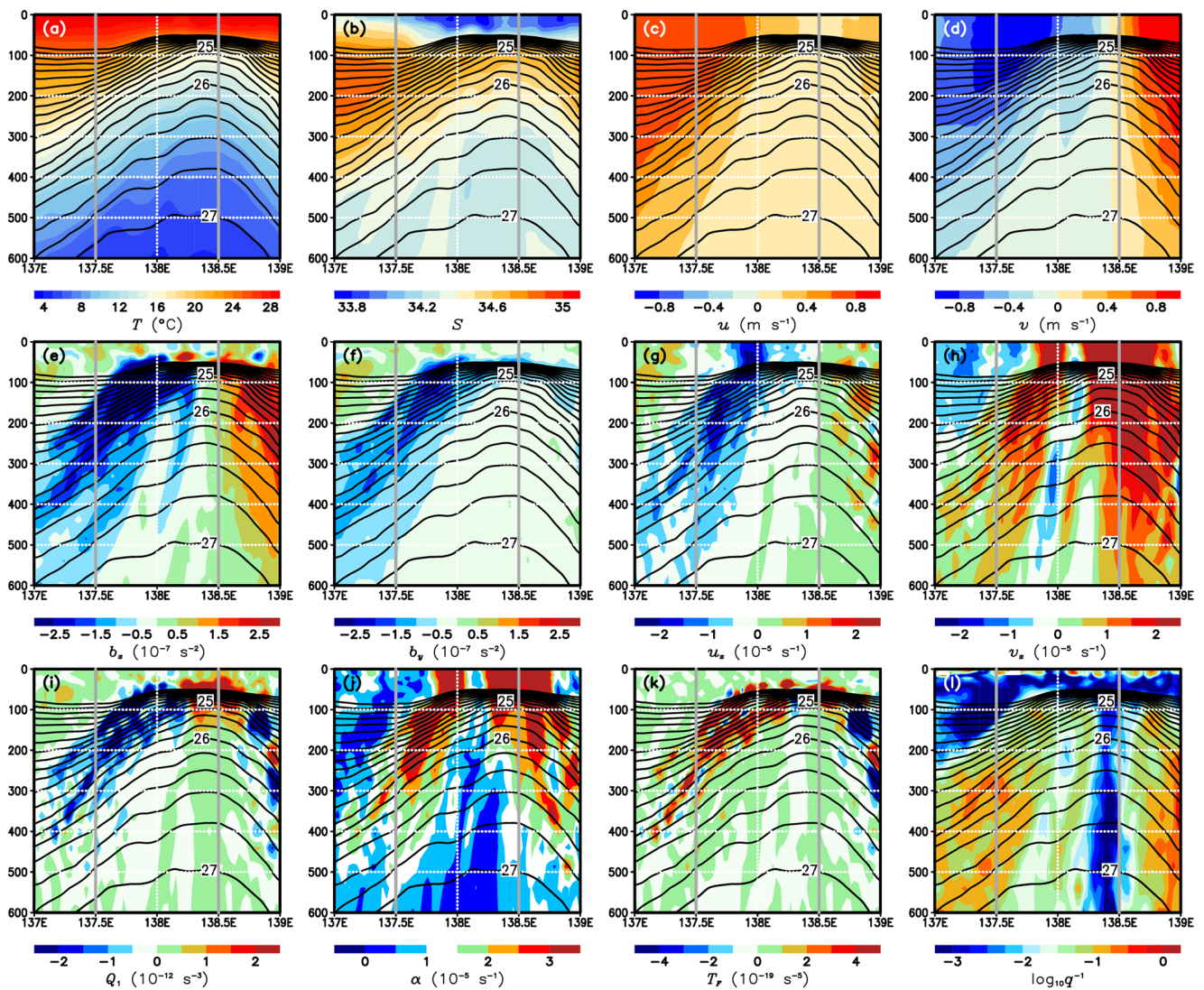


Figure 5. Sections of (a) T ($^{\circ}\text{C}$), (b) S , (c) u (m s^{-1}), (d) v (m s^{-1}), (e) b_x (10^{-7} s^{-2}), (f) b_y (10^{-7} s^{-2}), (g) u_x (10^{-5} s^{-1}), (h) v_x (10^{-5} s^{-1}), (i) Q_1 (10^{-12} s^{-3}) (j) α (10^{-5} s^{-1}) (k) T_r (10^{-19} s^{-5}), and (l) q^{-1} along $31^{\circ}50' \text{N}$ on 26 August 2019 in the reanalysis data set. Black lines denote σ_{θ} with a contour interval of 0.2 kg m^{-3} from 23 to 27 kg m^{-3} . Regions between gray lines denote observed area in the intensive survey.

The high-nitrate water was convex upward inshore north of $34^{\circ}15' \text{N}$ (Figure 6c), and the nitracline was largely along $24.0\sigma_{\theta}$. In contrast, near the Kuroshio front and in the southern peripheries of the anticyclonic eddy, the nitracline occurred at shallow depths across the isopycnals around 32° and $33^{\circ}15' \text{N}$, respectively (Figure 6c). This locally shallow high-nitrate water was accompanied by large CHL_{SCM} with shallow Z_{SCM} ; that is, CHL_{SCM} values were larger than $0.8 \mu\text{g L}^{-1}$ around a depth of 50 m (Figure 6d). Similar to the intensive survey, the high CHL_{SCM} was in the large- α area (Figure 1b) and near but not just below the high FSLE (Figure 1d). Regarding the surface front related to the fresh water (Figure 6b), the contribution to upward nutrient transport was considered to be much smaller than that of mesoscale front in deeper layer because the nutrient in the surface layer is depleted during summer and fall.

General trends in the physical and biological data from all 10 surveys were examined to investigate how frequently CHL_{SCM} increased near the fronts (Figure 7). As the maximum value of b_y related to the mesoscale front was usually located near a depth of 300 m (Figure 6b), we identified the positions of fronts by large positive and negative b_y at a depth of 300 m (Figure 7a). All sections captured the Kuroshio front as a large negative b_y that moved south over time (Figure 7a), associated with the transition of the Kuroshio into the large meander period from August 2017 (Kawabe, 1985, 1995). In addition, the section in August 2017 captured the fronts at the northern

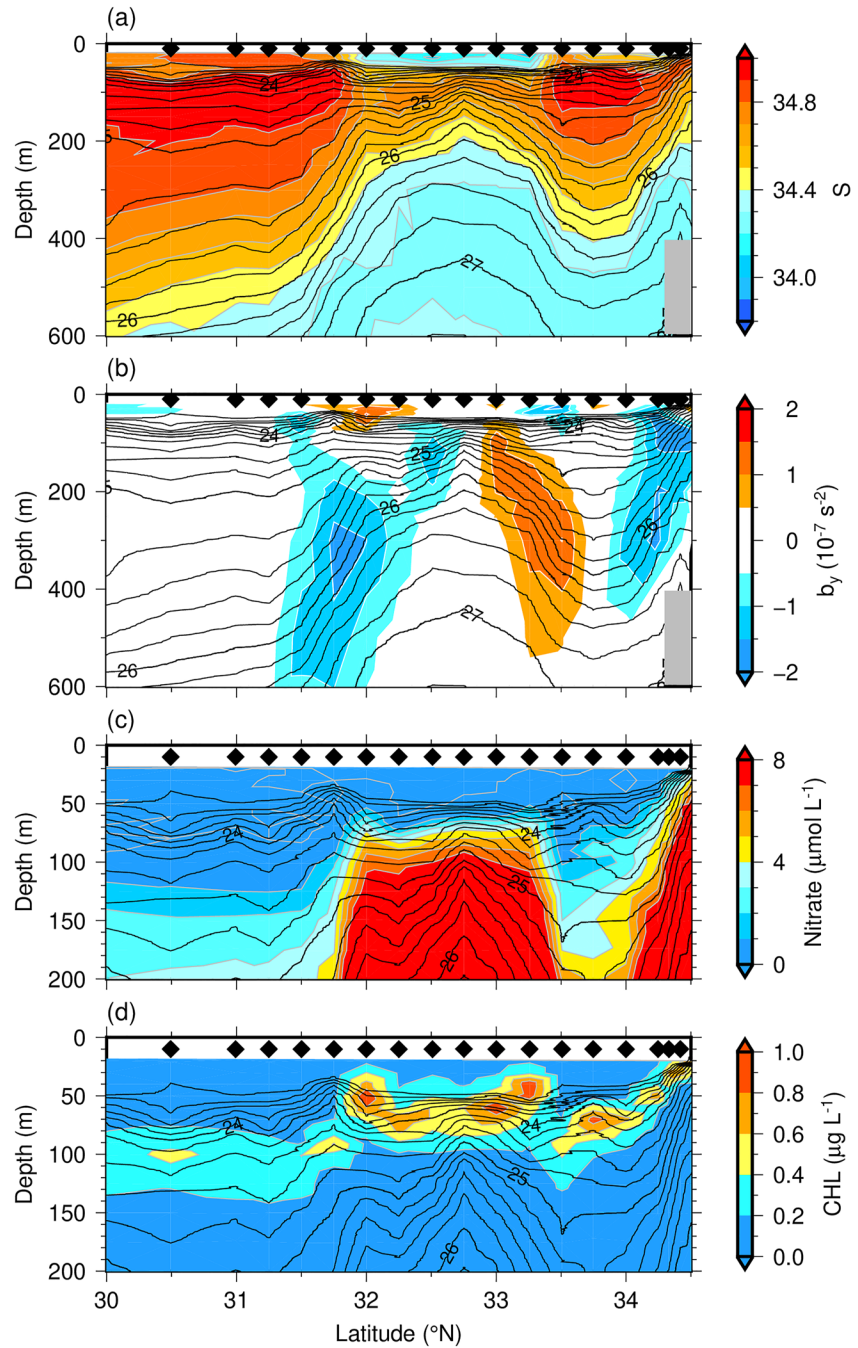


Figure 6. Sections of (a) S , (b) b_y (10^{-7} s^{-2}), (c) nitrate ($\mu\text{mol L}^{-1}$), and (d) CHL ($\mu\text{g L}^{-1}$) along 138°E in August 2017. Black diamonds at the top of the panel indicate the locations of CTD stations. Black lines denote σ_θ with a contour interval of 0.2 kg m^{-3} from 23 to 27 kg m^{-3} .

and southern peripheries of the anticyclonic mesoscale eddy as described above, and the section in November 2017 recorded the front associated with another warm water mass that flowed into the inshore region (not shown) as a positive b_y close to the coast at 34°N (Figure 7a). Thus, the repeat survey traversed the Kuroshio front 10 times and the front at the periphery of the warm water mass 3 times.

We now assume that the dynamical processes that lead to the shoaling of the nitracline near the fronts, such as frontogenesis and the resulting mixing, occur frequently. This assumption is reasonable in this region where there are active frontal and eddy fluctuations that interact. Large, shallow CHL_{SCM} values are expected in association

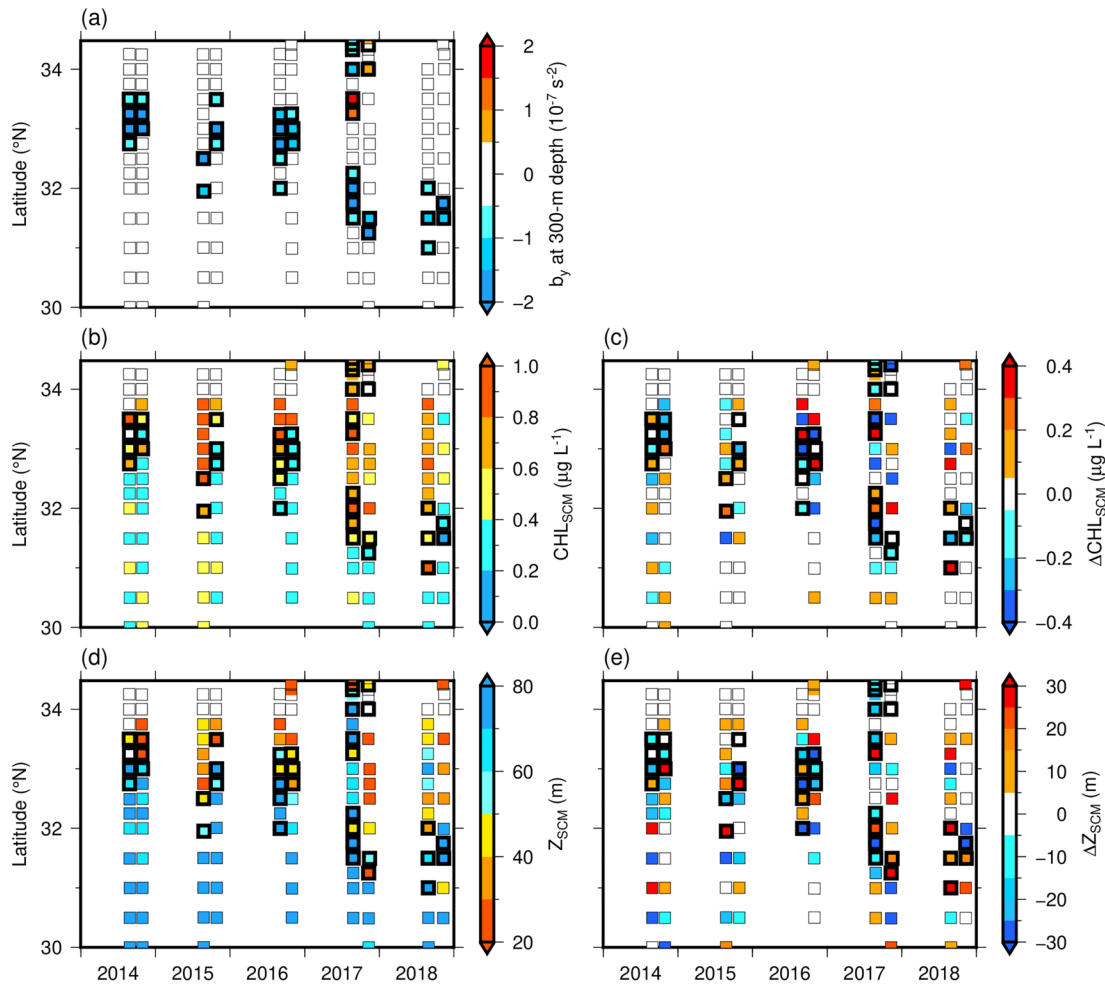


Figure 7. Temporal changes in the distribution and value of (a) b_y at a depth of 300 m (10^{-7} s^{-2}), (b) CHL_{SCM} ($\mu\text{g L}^{-1}$), (c) $\Delta\text{CHL}_{\text{SCM}}$ ($\mu\text{g L}^{-1}$), (d) Z_{SCM} (m), and (e) ΔZ_{SCM} (m). Dark squares denote fronts detected by b_y at a depth of 300 m.

with frontal structures. On the scale of crossing the Kuroshio (30–34°N), the values of CHL_{SCM} were large, and those of Z_{SCM} were shallow in the inshore water (Figures 7b and 7d). Focusing on the frontal region, their large and shallow horizontal extrema were usually recognized (Figures 7b and 7d). To identify the variation of the CHL_{SCM} and Z_{SCM} near the front, horizontal gradients of CHL_{SCM} and Z_{SCM} were calculated (Figures 7c and 7e). Large positive values of the meridional gradient in CHL_{SCM} ($\Delta\text{CHL}_{\text{SCM}}$) were found associated with the fronts, with accompanying negative values immediately north of them (Figure 7c); that is, CHL_{SCM} locally increased near the front. At the same time, the meridional gradient of Z_{SCM} (ΔZ_{SCM} ; positive values denote a shallow Z_{SCM} toward the north) was mostly positive when $\Delta\text{CHL}_{\text{SCM}}$ was positive (Figures 7c and 7e). The positive values of ΔZ_{SCM} near the front were often between negative values (Figure 7e); Z_{SCM} tended to be deep both north and south of the area where CHL_{SCM} increased. As a result, 11 out of 13 (85%) fronts (with the exception of two unclear fronts near the coast that were associated with a warm water mass in August and November 2017) were accompanied by an increase in CHL_{SCM} and a shallow Z_{SCM} . Stations where large absolute b_y values were calculated were close to those where large CHL_{SCM} values were observed at shallow depths.

3.4. Empirical Model Analyses

The relationships between the frontal structure, the shoaling of the nitracline, and the increase in CHL_{SCM} were examined using 174 profiles obtained from the repeat surveys. There was a positive correlation between Z_{NI} and Z_{SCM} (t -value = 18.2, p -value < 0.001) from each profile (Figure 8a). As anticipated, the shallower the nitracline, the shallower is Z_{SCM} . The values of CHL_{SCM} were negatively correlated with Z_{NI} (t -value = -12.7,

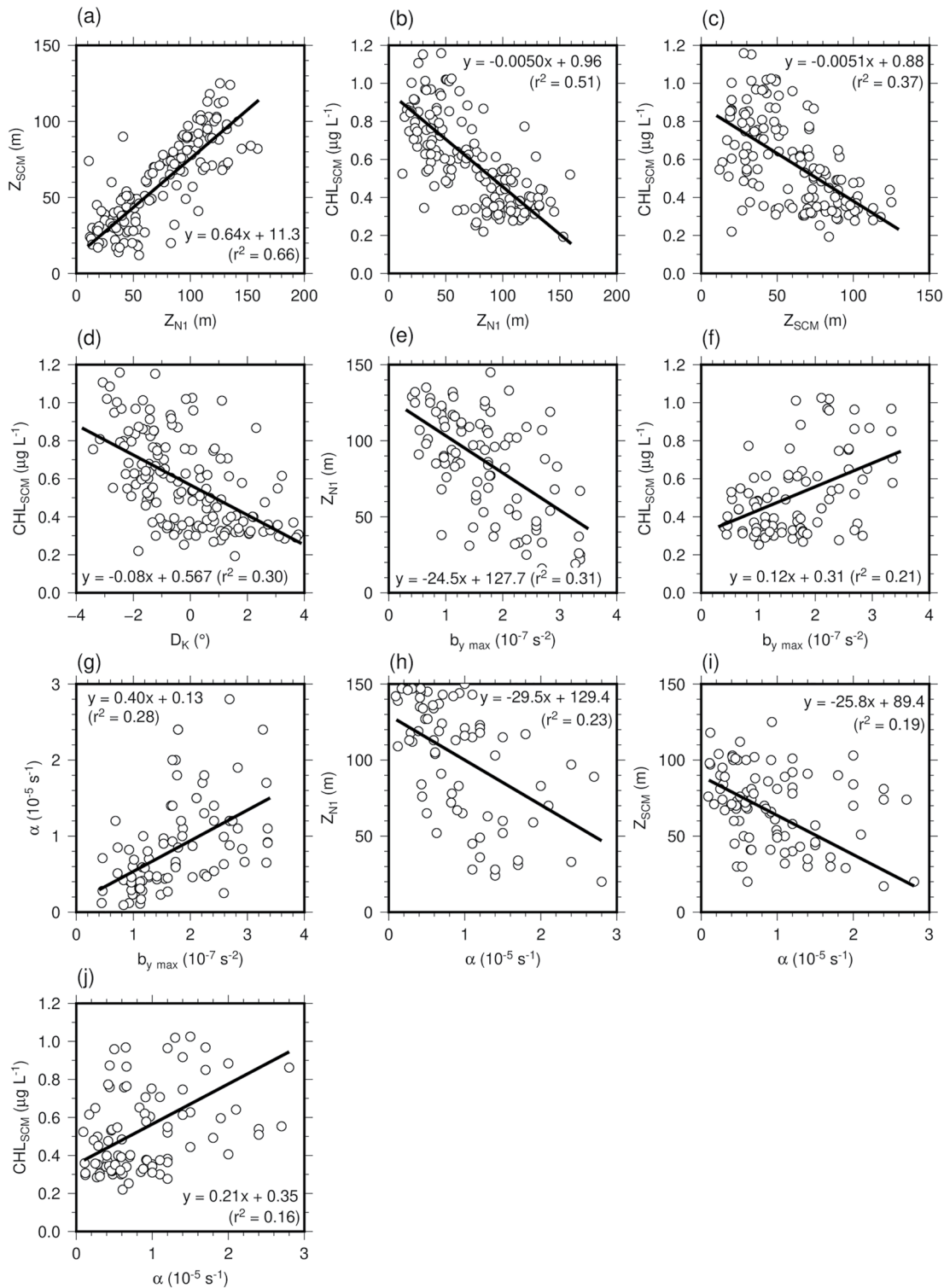


Figure 8. Relationship between (a) Z_{N1} (m) and Z_{SCM} (m), (b) Z_{N1} (m) and CHL_{SCM} ($\mu\text{g L}^{-1}$), (c) Z_{SCM} (m) and CHL_{SCM} ($\mu\text{g L}^{-1}$), (d) D_K ($^\circ$) and CHL_{SCM} ($\mu\text{g L}^{-1}$), (e) $b_{y \max}$ (10^{-7} s^{-2}) and Z_{N1} (m), (f) $b_{y \max}$ (10^{-7} s^{-2}) and CHL_{SCM} ($\mu\text{g L}^{-1}$), (g) $b_{y \max}$ (10^{-7} s^{-2}) and α (10^{-5} s^{-1}), (h) α (10^{-5} s^{-1}) and Z_{N1} (m), (i) α (10^{-5} s^{-1}) and Z_{SCM} (m), and (j) α (10^{-5} s^{-1}) and CHL_{SCM} ($\mu\text{g L}^{-1}$).

Table 2
The Results of GLMs

	Coefficient ± SE	<i>t</i> -value	<i>p</i> -value	ΔDE
(a) $Z_{SCM} \sim \text{glm}(\text{SSH} + b_{y \max} + \alpha + \beta)$				
β	21.67 ± 3.89	5.588	1.04×10^{-7}	
$b_{y \max} \times 10^5$	-7.42 ± 1.32	-5.62	8.90×10^{-8}	7%
$\alpha \times 10^6$	-3.79 ± 2.17	-1.75	0.0822	1%
SSH	0.399 ± 0.030	13.154	$<2 \times 10^{-16}$	39%
(b) $Z_{SCM} \sim \text{glm}(Z_{N1} + b_{y \max} + \alpha + D_K + \beta)$				
β	25.8 ± 3.5	7.3	1.53×10^{-11}	
$b_{y \max} \times 10^5$	-2.46 ± 1.40	-1.755	0.0812	0%
$\alpha \times 10^6$	-4.38 ± 1.60	-2.749	0.0067	1%
D_K	1.85 ± 0.98	1.894	0.0601	1%
Z_{N1}	0.533 ± 0.042	12.576	$<2 \times 10^{-16}$	25%

Note. Coefficient with standard error (SE) of remained parameter, *t* value, *p*-value and ΔDE (a) The results of the least-AIC GLM including SSH (cf. Equation 5). and (b) those of the least-AIC GLM including Z_{N1} (Equation 6).

p-value <0.001; Figure 8b). Moreover, Z_{SCM} had a negative correlation with CHL_{SCM} (*t*-value = -9.3, *p*-value <0.001; Figure 8c); the shallower Z_{SCM} is, the larger CHL_{SCM} is. These relationships reflect not only the phenomena near the front but also the mesoscale structures such as difference of nitracline depth along the isopycnals between the inshore and offshore of the Kuroshio. The relationship between D_K and CHL_{SCM} showed such regional features; CHL_{SCM} is small (large) south (north) of the Kuroshio axis (*t*-value = -8.2, *p*-value <0.001; Figure 8d). The rough CHL distribution around the Kuroshio can be estimated when the Kuroshio axis is deduced from satellite observations even if the nutrient distribution in the ocean interior is unknown.

We estimated location and strength of the front as $b_{y \max}$. The extrema of $b_{y \max}$ near the surface related to the fresh water from inshore (Figure 6b) was eliminated to focus on mesoscale frontal structure. The $b_{y \max}$ depths were usually shallower than 400 m. It can be shown that Z_{N1} is negatively correlated with $b_{y \max}$ (*t*-value = -6.4, *p*-value <0.001), and CHL_{SCM} (*t*-value = 4.8, *p*-value <0.001) positively (Figures 8e and 8f). These relationships were different from those between the distance from the Kuroshio axis (i.e., $|D_K|$) and CHL_{SCM} (not shown, but can be deduced from Figure 8d). The relationship with $b_{y \max}$ shows not just the regional features that CHL_{SCM} is small (large) south (north) of the Kuroshio but the influence of the strength of the fronts on the distribution of nitrate and CHL_{SCM} .

The distribution of surface frontogenesis is broadly estimated as α and FSLE from SSH (Figure 1). When dynamical surface features obtained from satellite observation are linked with physical data in the ocean interior, the satellite information may enable SCM distribution in the subsurface layer to be estimated. While the FSLE detected sharp submesoscale structure (Figure 1d), it does not strictly correspond to the subsurface frontal structure and SCM as mentioned above. Although the spatial resolution was lower, we examined the relationship between the deformation field identified by α and SCM by considering the lateral extent of SCM. First, we examined the relationship between $b_{y \max}$ and α to link the surface and interior structure. The value of α at the nearest grid point to the profile was positively correlated with $b_{y \max}$ (*t*-value = 5.8, *p*-value <0.001; Figure 8g) despite the difference in spatiotemporal resolution between in-situ and satellite observations. Although the deformation flow detected by α can cause both frontogenesis and frontolysis, the strong deformation tends to occur in association with strong fronts detected by $b_{y \max}$. Therefore, the value of α at the surface can be related to the SCM distribution similar to the $b_{y \max}$. The value of α was negatively correlated to Z_{N1} (*t*-value = -4.6, *p*-value <0.001; Figure 8h) and Z_{SCM} (*t*-value = -4.3, *p*-value <0.001; Figure 8i). At a fixed α , Z_{N1} is estimated realistically to be deeper than Z_{SCM} . The value of α was also positively related to CHL_{SCM} (*t*-value = 3.9, *p*-value <0.001; Figure 8j), as follows:

$$CHL_{SCM} = 0.21 \times 10^5 \times \alpha + 0.35, r^2 = 0.16. \quad (10)$$

These relationships suggest that CHL_{SCM} is large and Z_{SCM} is shallow near the evolving fronts that have been identified by the SSH data albeit with a small coefficient of determination.

The least-AIC GLM using SSH as the explanatory variable (Equation 5) was not include D_K (Table 2a), and that using Z_{N1} was the full model (i.e., Equation 6; Table 2b). The DE values of the models were >62.8%. The detailed results of GLMs were summarized in Table 2. The coefficient values of $b_{y \max}$ was significantly negative in the GLM using SSH, indicating Z_{SCM} decrease with increasing $b_{y \max}$. The coefficient of α was not significant in this GLM, but remained in the optimal model and explained approximately 1% of Z_{SCM} variations. When using Z_{N1} instead of SSH, the coefficient of α was significantly negative. An increase in α has the effect of making the estimate of Z_{SCM} shallower. The prediction of SCM distribution in the ocean interior could be improved by adding a dynamic indicator of temporal change in the fronts from satellite data in addition to the quantities captured in snapshots such as ship observations, although there are issues of spatial resolution and non-geostrophic flow components.

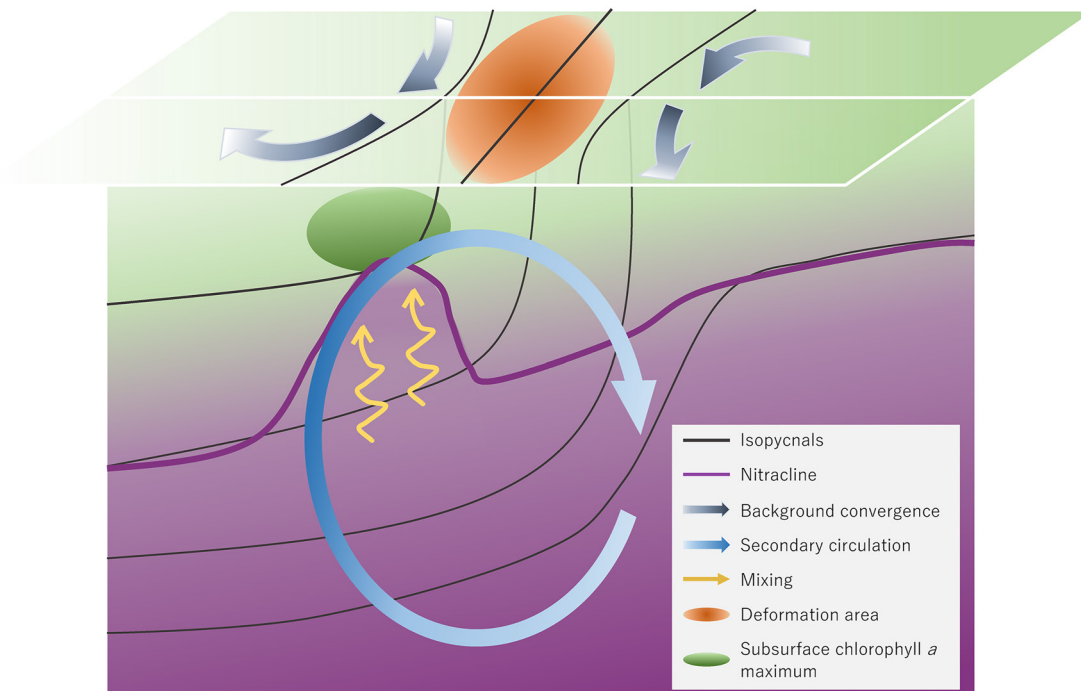


Figure 9. Schematic of the nutrient supply and increase of CHL_{SCM} caused by evolution of the fronts driven by mesoscale deformation flow. Black and purple lines denote isopycnals and a nitracline, respectively. Gray, blue, and yellow arrows show background flow causing convergence, secondary circulation associated with frontogenesis, and mixing caused by such as turbulence and SI. Orange and green circles indicate areas of large deformation and CHL_{SCM} . Green and purple colors show background CHL and nutrients.

4. Discussion

4.1. Processes Causing Nutrient Supply

The surface strain, FSLE, and the convergence of the interior velocity in the cross-front direction (Figures 1a, 1c, and 2c, 2d) and the growth of horizontal buoyancy gradient in the reanalysis data set (Figures 4 and 5) suggests that frontogenesis occurred during the intensive survey; that is, frontogenesis and the resulting secondary circulation were expected to cause the shoaling of the nitracline. The shoaling of the nitracline on the less dense side of the evolving front was consistent with the direction of the secondary circulation during frontogenesis (e.g., Hoskins, 1982; McWilliams et al., 2009; Thomas et al., 2008). In contrast to the downward transport of a water mass on the dense side of an evolving fronts, as reported near the Gulf Stream (Thomas & Joyce, 2010) and at the periphery of the mesoscale eddy north of the Kuroshio Extension (Ito et al., 2021), the high-resolution observations in this study have probably captured the upward transport of a water mass associated with frontogenesis.

The vertical water mass transport during frontogenesis that was reported by previous studies was largely along isopycnals (Ito et al., 2021; Thomas & Joyce, 2010). In contrast, the present results show a diapycnal nutrient supply in addition to one along isopycnals. High-NO water was supplied to the shallower layer near the front (Figure 3c). The water mass characteristics suggested that this high-NO water was not advected horizontally from inside the Kuroshio front, but was supplied vertically from the layer below. Therefore, turbulent mixing triggered by such as frontogenesis and the resulting secondary circulation and their interaction with internal waves (Kaneko et al., 2012; Nagai et al., 2009; Nagai et al., 2012) might have had a strong effect on the vertical transport of nutrients (Kaneko et al., 2013; Nagai & Clayton, 2017; Nagai et al., 2017; Nagai et al., 2019). In addition, reanalysis data set showed that q^{-1} was reasonably large (~ 0.3) near the Kuroshio front, implying the contribution of SI. The value of F was estimated to be $1.1 \times 10^{-6} \text{ mmol N m}^{-2} \text{ s}^{-1}$, using Equation 3. This is one order of magnitude larger than that at the same depth outside the Kuroshio front, and of the same order of magnitude as that reported near the Kuroshio front (Kaneko et al., 2013). This approach suggests that the turbulent mixing contributes to the shoaling of the nitracline near the evolving fronts. Again, the turbulence intensity has large spatiotemporal variation although that was not considered in this analysis.

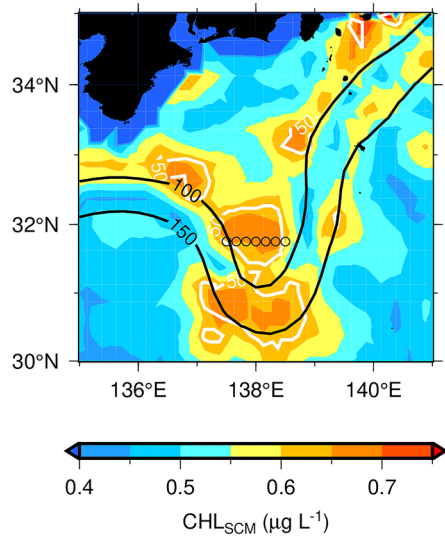


Figure 10. Distribution of CHL_{SCM} ($\mu\text{g L}^{-1}$) estimated from α on 26 August 2019. Open circles indicate the CTD stations. Black lines denote satellite sea surface height with a contour interval of 50 cm. White lines show the locations where $Z_{\text{SCM}} = 50$ m.

The nutrient supply and increase of CHL_{SCM} caused by evolution of the fronts are illustrated in Figure 9. Mesoscale background flow generates the convergence in the cross-front direction and the deformation (extracted as large α in this study) near the fronts (large $b_{y \text{ max}}$), resulting in the evolution of the fronts (frontogenesis). The secondary circulation associated with the frontogenesis causes upwelling (downwelling) on the less (more) dense side of the front. The upwelling flow and associated mixing triggered by such as turbulence and SI lead to shoaling of the nitracline. The shallow nitracline causes shallow Z_{SCM} and large CHL_{SCM} . A more thorough understanding of the dynamical processes involved in the vertical transport of nutrients and the distribution of SCM near fronts requires further observations and modeling, including both a comprehensive broad-scale view of the area and details of the small-scale structures near the front.

4.2. Estimation of Broad SCM Distribution

This study demonstrates that frontal structures and frontogenesis are related to the shoaling of the nitracline and an increase in the CHL_{SCM} . More generally, the contribution of various frontal structures to the SCM distribution can be deduced by analyzing observation data. Assuming that the physical and biological feature outlined in Section 3.4 are common throughout the study area, the distribution of the SCM is estimated from the surface α (Figure 10) using the relationship between biological properties and physical structure

observed in this study (Figure 8), albeit with some inherent uncertainties and small explanatory power of the single regression model ($r^2 < 0.2$). In the strong deformation (large α) near the front, both frontogenesis and frontolysis as seen in reanalysis data set (Figures 4a and 4j) and resulting secondary circulation and turbulent mixing are expected to lead to nutrient upwelling. Note that frontolysis also causes closed circulation opposite direction to frontogenesis (Hoskins, 1982). This vertical transport causes a shallow Z_{SCM} and large CHL_{SCM} . These processes are reflected in the relationship shown in Figure 8i, and the relationship enables us to evaluate Z_{SCM} from the surface α (the white line in Figure 10). As an example, we compared estimated values of Z_{SCM} and CHL_{SCM} with the observations from the intensive survey. Z_{SCM} on the western side of the front at $137^{\circ}50'E$ was 50 m (Figure 2h), which nearly matches the estimated value of 46 m (Figure 10). However, this approach predicted a shallow Z_{SCM} over a wider area (Figure 10) than is observed (Figure 2h). In addition, using the relationship with CHL_{SCM} (Figure 8j), the values of CHL_{SCM} were also estimated from surface α (color in Figure 10). Although the estimate of CHL_{SCM} was again for a wider area than was observed, the value was $0.6 \mu\text{g L}^{-1}$ (Figure 10), which was similar to the observed value of $0.5 \mu\text{g L}^{-1}$ (Figure 2h). The GLM analyses also showed the significance of α to estimate the distribution of CHL_{SCM} . In addition to accumulating in-situ data, further analyses for ocean conditions on multiple spatiotemporal scales are needed for a more detailed understanding of the contribution of such conditions on biological processes.

In frontal regions with large horizontal advection, shallowing of the nitracline caused by the upwelling flow and the rapid biological response do not occur at a fixed point, but are in motion. Since this Lagrangian perspective also applies to existing biological features, the observed increase in CHL concentrations should include the effect of the passive process (Lévy et al., 2018). Meanwhile, the high CHL_{SCM} was located near but not just below the large-FSLE regions (Figures 1c and 1d) probably because the submesoscale structure calculated at the surface had a spatial gap with mesoscale front in the ocean interior. The submesoscale-resolved deformation flow calculated at the surface seems to have a spatial gap with that in the ocean interior in the reanalysis data set (Figure 5j). Using α obtained from SSH, it is possible to quantify the increase in CHL_{SCM} over a wider area including both the region where frontogenesis occurs and further downstream region considering the spatial extent of the physical and biological processes. The estimates of Z_{SCM} and CHL_{SCM} were generally reasonable, but the area of shallow Z_{SCM} and large CHL_{SCM} values was overestimated compared with the in-situ observations (Figures 2g and 9). The overestimate is likely to be because of the resolution of the satellite altimeter, other processes that contribute to the variability in CHL, as well as the small explanatory power of the single regression model. A more detailed and accurate SCM distribution and biological productivity requires a relationship between higher-resolution data such as FSLE and physical and biological structure in the ocean interior.

4.3. Interannual Variation and Seasonality

Since the repeat survey revealed the effect of the fronts on the SCM distribution in the periods with and without the large meander of the Kuroshio, the affected area differs depending on the location of the Kuroshio (Figure 7). The Kuroshio moves off the south coast of Japan around 138°E during the Kuroshio large meander period (Figure 1a), whereas it flows along the coast during the nearshore period when there is no large meander (Kawabe, 1985, 1995). Especially during the unstable period of the Kuroshio, disturbances of the Kuroshio jet generate mesoscale eddies north and south of the Kuroshio front (Figure 1). Therefore, such mesoscale disturbances also affect the SCM distribution because of the accompanying frontal structure and the strain field (Figures 1 and 6), suggesting an impact of the stability of the Kuroshio.

In this study, we focused on physical and biological conditions during summer and fall, when the variability in the mixed layer has a lower impact on nutrient supplies than in winter and spring (Limsakul et al., 2001, 2002). However, although the front's impact on nutrient supplies is roughly an order of magnitude smaller than that from the development of the winter mixed layer in the subtropical gyre (Williams and McLaren, 2000), fronts can affect the biological distribution in winter and spring. In fact, a visual inspection of all the survey data (not shown) identified increases in CHL at the surface, likely because of the existence of fronts. Dedicated observations near the fronts are needed over every season to quantify the contribution from each process to the nutrient supply into the euphotic layer.

5. Summary

In this study, we described the contribution that fronts and frontogenesis make to the shoaling of the nitracline and SCM distribution using an intensive survey, seasonal repeat surveys, and satellite observations, alongside high-resolution reanalysis data set. The intensive survey used both biological and physical parameters to show that the shoaling of high nitrate (large NO value) water and a large CHL_{SCM} was near the evolving Kuroshio front. The high-resolution data set supported the interpretation that the Kuroshio front was in the process of frontogenesis during the intensive survey. The repeat surveys along 138°E in summer and fall also identified the relationship between the fronts, the shoaling of the nitracline, and the increase in CHL_{SCM} . Values of Z_{SCM} were shallow and those of CHL_{SCM} were large when strong fronts existed. The lateral strain rate obtained from the satellite SSH (i.e., α) was also related to the CHL_{SCM} ; that is, the larger the value of α , the shallower Z_{SCM} and larger CHL_{SCM} are. The GLMs demonstrated that it is statistically valid to use the satellite-derived geostrophic velocity field to estimate the SCM distribution.

The upwelling of nitrate along isopycnals appears to be caused by frontogenesis and resulting secondary circulation, judging from the convergent flow in the cross-front direction, the satellite-derived strain and FSLE, and evidence of frontogenesis from reanalysis data set. In addition, vertical diffusion contributed to the diapycnal nutrient supply. It is reasonable to assume that frontogenesis and the resulting mixing processes occur frequently in this region, which further emphasizes the relationship between fronts and SCM distribution. Our surveys and analysis suggest that fronts and frontogenesis have an impact on SCM distribution, and that physical data can be used to estimate the distribution in the ocean interior. This study also shows that further work is needed to elucidate the relationship between fronts, SCM distribution, and biological productivity in different regions and seasons. Continuous high-resolution in-situ and satellite observations as well as modeling are required to further reveal the detailed physical and biological processes occurring near fronts.

Data Availability Statement

All physical and part of biological data obtained from surveys in this study are available from Mendeley Data (<https://doi.org/10.17632/fnhny2sd5b.1>). The remaining biological data (obtained in 2018 and 2019) is restricted by the regulations of Fisheries Resources Institute for five years after obtaining the data from the surveys. This is available in (<https://doi.org/10.17632/7byj7cxctk.1>) with the approval of the institute, and is not accessible to the public or research community until September 2024. To obtain data access approval from the institute, please contact the corresponding author.

Acknowledgments

We thank the captains, officers, crew member, and scientists of the R/V *Soyomaru* cruise for their cooperation. We are grateful to two anonymous reviewers for their helpful comments. This work was financially supported by the Ministry of Agriculture, Forestry and Fisheries, Japan through Grants from study on “Establishing a network of environment and fisheries information” and “Marine Fisheries stock assessment and evaluation for Japanese, the Fisheries Agency of Japan.”

References

- Broecker, W. S. (1974). “NO”, a conservative water-mass tracer. *Earth and Planetary Science Letters*, 23(1), 100–107. [https://doi.org/10.1016/0012-821x\(74\)90036-3](https://doi.org/10.1016/0012-821x(74)90036-3)
- Capet, X., McWilliams, J. C., Molemaker, M. J., & Shchepetkin, A. F. (2008a). Mesoscale to submesoscale transition in the California current system, part II: Frontal processes. *Journal of Physical Oceanography*, 38(1), 44–64. <https://doi.org/10.1175/2007JPO3672.1>
- Capet, X., McWilliams, J. C., Molemaker, M. J., & Shchepetkin, A. F. (2008b). Mesoscale to submesoscale transition in the California Current System. Part I: Flow structure, eddy flux, and observational tests. *Journal of Physical Oceanography*, 38(1), 29–43. <https://doi.org/10.1175/2007JPO3671.1>
- Capet, X., McWilliams, J. C., Molemaker, M. J., & Shchepetkin, A. F. (2008c). Mesoscale to submesoscale transition in the California current system. Part III: Energy balance and flux. *Journal of Physical Oceanography*, 38(10), 2256–2269. <https://doi.org/10.1175/2008JPO3810.1>
- Claustre, H., Kerhervé, P., Marty, J. C., Prieur, L., Videau, C., & Hecq, J.-H. (1994). Phytoplankton dynamics associated with a geostrophic front: Ecological and biogeochemical implications. *Journal of Marine Research*, 52(4), 711–742. <https://doi.org/10.1357/0022240943077000>
- Cullen, J. J. (2015). Subsurface chlorophyll maximum layers: Enduring enigma or mystery solved? *Annual Review of Marine Science*, 7(1), 207–239. <https://doi.org/10.1146/annurev-marine-010213-135111>
- Cullen, J. J., & Eppley, R. W. (1981). Chlorophyll maximum layers of the Southern California Bight and possible mechanisms of their formation and maintenance. *Oceanologica Acta*, 4, 23–31.
- D’Asaro, E. A., Lee, C., Rainville, L., Harcourt, R., & Thomas, L. N. (2011). Enhanced turbulence and energy dissipation at ocean fronts. *Science*, 332(6027), 318–322. <https://doi.org/10.1126/science.1201515>
- d’Ovidio, F., Fernandez, V., Hernandez-García, E., & López, C. (2004). Mixing structures in the mediterranean sea from finite-size Lyapunov exponents. *Geophysical Research Letters*, 31(17), L17203. <https://doi.org/10.1029/2004GL020328>
- Goericke, R., & Welschmeyer, N. A. (1998). Response of Sargasso Sea phytoplankton biomass, growth rates and primary production to seasonally varying physical forcing. *Journal of Plankton Research*, 20(12), 2223–2249. <https://doi.org/10.1093/plankt/20.12.2223>
- Gula, J., Molemaker, M. J., & McWilliams, J. C. (2014). Submesoscale cold filaments in the Gulf Stream. *Journal of Physical Oceanography*, 44(10), 2617–2643. <https://doi.org/10.1175/JPO-D-14-0029.1>
- Hales, B., Hebert, D., & Marra, J. (2009). Turbulent supply of nutrients to phytoplankton at the New England shelf break front. *Journal of Geophysical Research*, 114(C5), C05010. <https://doi.org/10.1029/2008JC005011>
- Hirose, N., Sakamoto, K., Usui, N., Yamanaka, G., & Kohno, N. (2020). The 10-year reanalysis dataset of an operational system for monitoring and forecasting coastal and open-ocean status around Japan (JPN Atlas 2020) Technical reports of the Meteorological Research Institute (Vol. 83). <https://doi.org/10.11483/mritechrepo.83>
- Hirose, N., Usui, N., Sakamoto, K., Tsujino, H., Yamanaka, G., Nakano, H., et al. (2019). Development of a new operational system for monitoring and forecasting coastal and open-ocean states around Japan. *Ocean Dynamics*, 69(11–12), 1333–1357. <https://doi.org/10.1007/s10236-019-01306-x>
- Hoskins, B. J. (1974). The role of potential vorticity in symmetric stability and instability. *Quarterly Journal of the Royal Meteorological Society*, 100(425), 480–482. <https://doi.org/10.1002/qj.49710042520>
- Hoskins, B. J. (1982). The mathematical theory of frontogenesis. *Annual Review of Fluid Mechanics*, 14(1), 131–151. <https://doi.org/10.1146/annurev.fl.14.010182.001023>
- Ito, D., Kodama, T., Shimizu, Y., Setou, T., Hidaka, K., Ambe, D., & Sogawa, S. (2023a). All physical and part of biological data for Frontogenesis elevates the maximum chlorophyll *a* concentration at the subsurface near the Kuroshio during well-stratified seasons [dataset]. Mendeley Data. <https://doi.org/10.17632/fnhny2sd5b.1>
- Ito, D., Kodama, T., Shimizu, Y., Setou, T., Hidaka, K., Ambe, D., & Sogawa, S. (2023b). Restricted biological data for Frontogenesis elevates the maximum chlorophyll *a* concentration at the subsurface near the Kuroshio during well-stratified seasons [dataset]. Mendeley Data. <https://doi.org/10.17632/7byj7cxctk.1>
- Ito, D., Suga, T., Kouketsu, S., Oka, E., & Kawai, Y. (2021). Spatiotemporal evolution of submesoscale filaments at the periphery of an anticyclonic mesoscale eddy north of the Kuroshio Extension. *Journal of Oceanography*, 77(5), 763–780. <https://doi.org/10.1007/s10872-021-00607-4>
- Itoh, S., Tsutsumi, E., Masunaga, E., Sakamoto, T. T., Ishikawa, K., Yanagimoto, D., et al. (2022). Seasonal cycle of the confluence of the tsugaru warm, oyashio, and Kuroshio currents east of Japan. *Journal of Geophysical Research: Oceans*, 127(8), e2022JC018556. <https://doi.org/10.1029/2022JC018556>
- Joyce, T. M. (1989). On in situ “calibration” of shipboard ADCPs. *Journal of Atmospheric and Oceanic Technology*, 6(1), 169–172. [https://doi.org/10.1175/1520-0426\(1989\)006<0169:OISOSA>2.0.CO;2](https://doi.org/10.1175/1520-0426(1989)006<0169:OISOSA>2.0.CO;2)
- Kaneko, H., Yasuda, I., Komatsu, K., & Itoh, S. (2012). Observations of the structure of turbulent mixing across the Kuroshio. *Geophysical Research Letters*, 39(15), L15602. <https://doi.org/10.1029/2012GL052419>
- Kaneko, H., Yasuda, I., Komatsu, K., & Itoh, S. (2013). Observations of vertical turbulent nitrate flux across the Kuroshio. *Geophysical Research Letters*, 40(12), 3123–3127. <https://doi.org/10.1002/grl50613>
- Kawabe, M. (1985). Sea level variations at the Izu Islands and typical stable paths of the Kuroshio. *Journal of the Oceanographical Society of Japan*, 41(5), 307–326. <https://doi.org/10.1007/BF02109238>
- Kawabe, M. (1995). Variations of current path, velocity, and volume transport of the Kuroshio in relation with the large meander. *Journal of Physical Oceanography*, 25(12), 3103–3117. [https://doi.org/10.1175/1520-0485\(1995\)025<3103:VOCPPA>2.0.CO;2](https://doi.org/10.1175/1520-0485(1995)025<3103:VOCPPA>2.0.CO;2)
- Kimura, S., Kasai, A., Nakata, H., Sugimoto, T., Simpson, J. H., & Cheok, J. V. S. (1997). Biological productivity of mesoscale eddies caused by frontal disturbances in the Kuroshio. *ICES Journal of Marine Science*, 54(2), 179–192. <https://doi.org/10.1006/jmsc.1996.0209>
- Kimura, S., Nakata, H., & Okazaki, Y. (2000). Biological production in meso-scale eddies caused by frontal disturbances of the Kuroshio Extension. *ICES Journal of Marine Science*, 57(1), 133–142. <https://doi.org/10.1006/jmsc.1999.0564>
- Klein, P., & Lapeyre, G. (2009). The oceanic vertical pump induced by mesoscale and submesoscale turbulence. *Annual Review of Marine Science*, 1, 351–375. <https://doi.org/10.1146/annurev.marine.010908.163704>
- Kodama, T., Ichikawa, T., Hidaka, K., & Furuya, K. (2015). A high sensitive and large concentration range colorimetric continuous flow analysis for ammonium concentration. *Journal of Oceanography*, 71(1), 65–75. <https://doi.org/10.1007/s10872-014-0260-6>
- Kodama, T., Shimizu, Y., Ichikawa, T., Hiroe, Y., Kusaka, A., Morita, H., et al. (2014). Seasonal and spatial contrast in the surface layer nutrient content around the Kuroshio along 138E, observed between 2002 and 2013. *Journal of Oceanography*, 70(6), 489–503. <https://doi.org/10.1007/s10872-014-0245-5>
- Komatsu, K., & Hiroe, Y. (2019). Structure and impact of the Kuroshio nutrient stream. In T. Nagai, K. Suzuki, & M. Takahashi (Eds.), *Kuroshio current, physical, biogeochemical and ecosystem dynamics, Geophysical monograph 243* (pp. 85–104). John Wiley and Sons.

- Lapeyre, G., & Klein, P. (2006). Impact of the small-scale elongated filaments on the oceanic vertical pump. *Journal of Marine Research*, 64(6), 835–851. <https://doi.org/10.1357/002224006779698369>
- Lévy, M., Ferrari, R., Franks, P. J. S., Martin, A. P., & Rivère, P. (2012). Bringing physics to life at the submesoscale. *Geophysical Research Letters*, 39(14), L14602. <https://doi.org/10.1029/2012GL052756>
- Lévy, M., Franks, P. J. S., & Smith, K. S. (2018). The role of submesoscale currents in structuring marine ecosystems. *Nature Communications*, 9(1), 4758. <https://doi.org/10.1038/s41467-018-07059-3>
- Lévy, M., Klein, P., & Treguier, A.-M. (2001). Impact of sub-mesoscale physics on production and subduction of phytoplankton in an oligotrophic regime. *Journal of Marine Research*, 59(4), 535–565. <https://doi.org/10.1357/002224001762842181>
- Limsakul, A., Saino, T., Goes, J. I., & Midorikawa, T. (2002). Seasonal variability in the lower trophic level environments of the Western subtropical Pacific and oyashio waters—A retrospective study. *Deep Sea Research Part II*, 49(24–25), 5487–5512. [https://doi.org/10.1016/S0967-0645\(02\)00208-4](https://doi.org/10.1016/S0967-0645(02)00208-4)
- Limsakul, A., Saino, T., Midorikawa, T., & Goes, J. I. (2001). Temporal variations in lower trophic level biological environments in the northwestern North Pacific Subtropical Gyre from 1950 to 1997. *Progress in Oceanography*, 49(1–4), 129–149. [https://doi.org/10.1016/S0079-6611\(01\)00019-2](https://doi.org/10.1016/S0079-6611(01)00019-2)
- Mahadevan, A. (2016). The impact of submesoscale physics on primary productivity of plankton. *Annual Review of Marine Science*, 8(1), 161–184. <https://doi.org/10.1146/annurev-marine-010814-015912>
- Mahadevan, A., Thomas, L. N., & Tandon, A. (2008). Comment on “Eddy/wind interactions stimulate extraordinary mid-ocean plankton blooms”. *Science*, 320(5875), 448. <https://doi.org/10.1126/science.1152111>
- Masuda, T., Furuya, K., Kohashi, N., Sato, M., Takeda, S., Uchiyama, M., et al. (2010). Lagrangian observation of phytoplankton dynamics at an artificially enriched subsurface water in Sagami Bay, Japan. *Journal of Oceanography*, 66(6), 801–813. <https://doi.org/10.1007/s10872-010-0065-1>
- McWilliams, J. C. (2016). Submesoscale currents in the ocean. *Proceedings of the Royal Society A: Mathematical, Physical and Engineering Sciences*, 472(2189), 1–32. <https://doi.org/10.1098/rspa.2016.0117>
- McWilliams, J. C., Colas, F., & Molemaker, M. J. (2009). Cold filamentary intensification and oceanic surface convergence lines. *Geophysical Research Letters*, 36(18), L18602. <https://doi.org/10.1029/2009GL039402>
- Mensa, J. A., Garraffo, Z., Griffa, A., Özgökman, T. M., Haza, A., & Veneziani, M. (2013). Seasonality of the submesoscale dynamics in the Gulf Stream region. *Ocean Dynamics*, 63(8), 923–941. <https://doi.org/10.1007/s10236-013-0633-1>
- Miller, J. E. (1948). On the concept of frontogenesis. *Journal of Meteorology*, 5(4), 169–171. [https://doi.org/10.1175/1520-0469\(1948\)005<0169:OTCOF>2.0.CO;2](https://doi.org/10.1175/1520-0469(1948)005<0169:OTCOF>2.0.CO;2)
- Morel, A. (1988). Optical modeling of the upper ocean in relation to its biogenous matter content (Case I waters). *Journal of Geophysical Research*, 93(C9), 10749–10768. <https://doi.org/10.1029/JC093iC09p10749>
- Munk, W., Armi, L., Fischer, K., & Zachariassen, F. (2000). Spirals on the sea. *Proceedings of the Royal Society A: Mathematical, Physical and Engineering Sciences*, 456(1997), 1217–1280. <https://doi.org/10.1098/rspa.2000.0560>
- Nagai, T., & Clayton, S. (2017). Nutrient interleaving below the mixed layer of the Kuroshio Extension front. *Ocean Dynamics*, 67(8), 1027–1046. <https://doi.org/10.1007/s10236-017-1070-3>
- Nagai, T., Durán, G. S., Otero, D. A., Mori, T., Yoshie, N., Ohgi, K., et al. (2019). How the Kuroshio Current delivers nutrients to sunlit layers on the Continental shelves with aid of near-inertial waves and turbulent. *Geophysical Research Letters*, 46(12), 6726–6735. <https://doi.org/10.1029/2019GL082680>
- Nagai, T., Hasegawa, D., Tanaka, T., Nakamura, H., Tsutsumi, E., Inoue, R., & Yamashiro, T. (2017). First evidence of coherent bands of strong turbulent layers associated with high-wavenumber internal-wave shear in the upstream Kuroshio. *Scientific Reports*, 7(1), 14555. <https://doi.org/10.1038/s41598-017-15167-1>
- Nagai, T., Tandon, A., Yamazaki, H., & Doubell, M. J. (2009). Evidence of enhanced turbulent dissipation in the frontogenetic Kuroshio Front thermocline. *Geophysical Research Letters*, 36(12), L12609. <https://doi.org/10.1029/2009GL038832>
- Nagai, T., Tandon, A., Yamazaki, H., Doubell, M. J., & Gallager, S. (2012). Direct observations of microscale turbulence and thermohaline structure in the Kuroshio Front. *Journal of Geophysical Research*, 117(C8), C08013. <https://doi.org/10.1029/2011JC007228>
- Okazaki, Y., Miyamoto, H., Suzuki, K., Saito, H., Hidaka, K., & Ichikawa, T. (2019). Diverse trophic pathways from zooplankton to larval and Juvenile Fishes in the Kuroshio ecosystem. In T. Nagai, K. Suzuki, & M. Takahashi (Eds.), *Kuroshio current, physical, biogeochemical and ecosystem dynamics*, *Geophysical monograph 243* (pp. 245–256). John Wiley and Sons.
- Osborn, T. R. (1980). Estimates of the local-rate of vertical diffusion from dissipation measurements. *Journal of Physical Oceanography*, 10(1), 83–89. [https://doi.org/10.1175/1520-0485\(1980\)010<0083:EOTLRO>2.0.CO;2](https://doi.org/10.1175/1520-0485(1980)010<0083:EOTLRO>2.0.CO;2)
- Perruche, C., Rivière, P., Lapeyre, G., Carton, X., & Pondaven, P. (2011). Effects of surface quasi-geostrophic turbulence on phytoplankton competition and coexistence. *Journal of Marine Research*, 69(1), 105–135. <https://doi.org/10.1357/002224011798147606>
- Richardson, K., Visser, A. W., & Pedersen, F. B. (2000). Subsurface phytoplankton blooms fuel pelagic production in the North Sea. *Journal of Plankton Research*, 22(9), 1663–1671. <https://doi.org/10.1093/plankt/22.9.1663>
- Rudnick, D. L. (1996). Intensive surveys of the Azores front: 2. Inferring the geostrophic and vertical velocity fields. *Journal of Geophysical Research*, 101(C7), 16291–16303. <https://doi.org/10.1029/96JC01144>
- Saijo, Y., Iizuka, S., & Asaoka, O. (1969). Chlorophyll maximum in Kuroshio and adjacent area. *Marine Biology*, 4(3), 190–196. <https://doi.org/10.1007/bf00393892>
- Saitoh, S., Kosaka, S., & Iisaka, J. (1986). Satellite infrared observations of Kuroshio warm-core rings and their application to study of Pacific saury migration. *Deep-Sea Research, Part A: Oceanographic Research Papers*, 33(11–12), 1601–1615. [https://doi.org/10.1016/0198-0149\(86\)90069-5](https://doi.org/10.1016/0198-0149(86)90069-5)
- Sasaki, H., Klein, P., Qiu, B., & Sasai, Y. (2014). Impact of oceanic-scale interactions on the seasonal modulation of ocean dynamics by the atmosphere. *Nature Communications*, 5(1), 5636. <https://doi.org/10.1038/ncomms6636>
- Sharples, J., Moore, C. M., Rippeth, T. P., Holligan, P. M., Hydes, D. J., Fisher, N. R., & Simpson, J. H. (2001). Phytoplankton distribution and survival in the thermocline. *Limnology & Oceanography*, 46(3), 486–496. <https://doi.org/10.4319/lo.2001.46.3.0486>
- Siegelman, L., Klein, P., Thompson, A. F., Torres, H. S., & Menemenlis, D. (2020). Altimetry-based diagnosis of deep-reaching sub-mesoscale ocean fronts. *Fluids*, 5(3), 145. <https://doi.org/10.3390/fluids5030145>
- Smith, K. M., Hamlington, P. E., & Fox-Kemper, B. (2016). Effects of submesoscale turbulence on ocean tracers. *Journal of Geophysical Research: Oceans*, 121(1), 908–933. <https://doi.org/10.1002/2015JC011089>
- Sugimoto, T., & Tameishi, H. (1992). Warm-core rings, streamers and their role on the fishing ground formation around Japan. *Deep-Sea Research, Part A: Oceanographic Research Papers*, 39, S183–S201. [https://doi.org/10.1016/S0198-0149\(11\)80011-7](https://doi.org/10.1016/S0198-0149(11)80011-7)

- Sugisaki, H., Nonaka, M., Ishizaki, S., Hidaka, K., Kameda, T., Hirota, Y., et al. (2010). Status and trends of the Kuroshio region, 2003–2008. In S. M. McKinnell & M. J. Dagg (Eds.), *Marine ecosystems of the North Pacific ocean, 2003–2008, PICES spec. Public Services, North Pacific Marine Science Organization* (Vol. 4, pp. 330–359).
- Suzuki, R., & Ishimaru, T. (1990). An improved method for the determination of phytoplankton chlorophyll using N,N-dimethylformamide. *Journal of the Oceanographical Society of Japan*, 46(4), 190–194. <https://doi.org/10.1007/BF02125580>
- Takahashi, M., Nakai, T., Ishimaru, T., Hasumoto, H., & Fujita, Y. (1985). Distribution of the subsurface chlorophyll maximum and its nutrient-light environment in and around the Kuroshio off Japan. *Journal of the Oceanographical Society of Japan*, 41(2), 73–80. <https://doi.org/10.1007/BF02109176>
- Takasuka, A., Kuroda, H., Okunishi, T., Shimizu, Y., Hirota, Y., Kubota, H., et al. (2014). Occurrence and density of Pacific saury *Cololabis saira* larvae and juveniles in relation to environmental factors during the winter spawning season in the Kuroshio Current system. *Fisheries Oceanography*, 23(4), 304–321. <https://doi.org/10.1111/fog.12065>
- Takasuka, A., Oozeki, Y., & Kubota, H. (2008). multi-species regime shifts reflected in spawning temperature optima of small pelagic fish in the Western North Pacific. *Marine Ecology Progress Series*, 360, 211–217. <https://doi.org/10.3354/meps07407>
- Tandon, A., & Nagai, T. (2019). Mixing associated with submesoscale processes. In J. K. Cochran, J. H. Bokuniewicz, & L. P. Yager (Eds.), *Encyclopedia of ocean science* (3rd ed., Vol. 3, pp. 567–577). <https://doi.org/10.1016/B978-0-12-409548-9.10952-2>
- Thomas, L. N., & Joyce, T. M. (2010). Subduction on the northern and southern flanks of the Gulf Stream. *Journal of Physical Oceanography*, 40(2), 429–438. <https://doi.org/10.1175/2009JPO4187.1>
- Thomas, L. N., Tandon, A., & Mahadevan, A. (2008). Submesoscale processes and dynamics. Ocean Modeling in an Eddy Regime. *Geophysical Monograph Series*, 177, 17–38. <https://doi.org/10.1029/177GM04>
- Thomas, L. N., Taylor, J. R., D'Asaro, E. A., Lee, C. M., Klymak, J. M., & Shcherbina, A. (2016). Symmetric instability, inertial oscillations, and turbulence at the Gulf Stream front. *Journal of Physical Oceanography*, 46(1), 197–217. <https://doi.org/10.1175/jpo-d-15-0008.1>
- Thomas, L. N., Taylor, J. R., Ferrari, R., & Joyce, T. M. (2013). Symmetric instability in the gulf stream. *Deep Sea Research Part II: Topical Studies in Oceanography*, 91, 96–110. <https://doi.org/10.1016/j.dsr2.2013.02.025>
- Thompson, L. (2000). Ekman Layers and two-dimensional frontogenesis in the upper ocean. *Journal of Geophysical Research*, 105(C3), 6437–6451. <https://doi.org/10.1029/1999JC900336>
- Tsujino, H., Urakawa, S., Nakano, H., Small, R. J., Kim, W. M., Yeager, S. G., et al. (2018). JRA-55 based surface dataset for driving ocean-sea-ice models (JRA55-do). *Ocean Modelling*, 130, 79–139. <https://doi.org/10.1016/j.ocemod.2018.07.002>
- Uda, M. (1938). Researches on “Shiome” or current rip in the seas and oceans. *Geophysical Magazine*, 11, 307–372.
- Videau, C. (1987). Primary production and physiological state of phytoplankton at the Ushant tidal front (west coast of Brittany, France). *Marine Ecology Progress Series*, 35, 141–151. <https://doi.org/10.3354/meps035141>
- Welschmeyer, N. A. (1994). Fluorometric analysis of chlorophyll *a* in the presence of chlorophyll *b* and phaeopigments. *Limnology & Oceanography*, 39(8), 1985–1992. <https://doi.org/10.4319/lo.1994.39.8.198>
- Weston, K., Fernand, L., Mills, D. K., Delahunty, R., & Brown, J. (2005). Primary production in the deep chlorophyll maximum of the central North Sea. *Journal of Plankton Research*, 27(9), 909–922. <https://doi.org/10.1093/plankt/fbi064>
- Williams, R. G., McLaren, A. J., & Follows, M. J. (2000). Estimating the convective supply of nitrate and implied variability in export production over the North Atlantic. *Global Biogeochemical Cycles*, 14(4), 1299–1313. <https://doi.org/10.1029/2000GB001260>
- Yanagi, T. (1987). Classification of “Siome”, streaks and fronts. *Journal of the Oceanographical Society of Japan*, 45(3), 149–158. <https://doi.org/10.1007/BF02109215>
- Yoder, J. A., Atkinson, L. P., Lee, T. N., Kim, H. H., & McClain, C. R. (1981). Roles of Gulf Stream frontal eddies in forming phytoplankton patches on the outer southeastern shelf. *Limnology & Oceanography*, 26(6), 1103–1110. <https://doi.org/10.4319/lo.1981.26.6.1103>